~~Characteristics~~ Modeling present and ~~evolution of~~ future bedrock permafrost distribution in the Sisimiut mountain area, West Greenland

Marco Marcer[1,2], Pierre-Allain Duvillard[3,4], Soňa Tomaškovičová[1], Steffen Ringsø Nielsen[2,5], André Revil[4], and Thomas Ingeman-Nielsen[1]

[1]DTU Sustain,Bygningstorvet, Bygning 115, 2800 Kgs. Lyngby, Denmark
[2]Arctic DTU, Siimuup Aqqutaa 32, B-1280, 3911 Sisimiut, Greenland
[3]Styx4D, 12 Allée du lac de Garde, Le Bourget du lac, France
[4]EDYTEM, Université Savoie Mont-Blanc, CNRS (UMR 5204), 73370 Le Bourget du Lac, France
[5]KTI Råstofskolen - Greenland School of Minerals and Petroleum, Adammip Aqq. 2, 3911 Sisimiut, Greenland

Correspondence: Marco Marcer (marcma@byg.dtu.dk)

Abstract. Bedrock permafrost is a feature of cold mountain ranges that was found responsible for the increase of rock fall and landslide activity in several regions across the globe. In Greenland, bedrock permafrost has received so far little attention from the scientific community, despite mountains are a predominant feature on the ice-free coastline and landslide activity is significant. With this study, we aim to move a first step towards the characterization of bedrock permafrost in Greenland. Our study area covers 100 km^2 of mountain terrain around the town of Sisimiut – 68° N on the West Coast. We first acquire ~~surface ground temperature data from 2020-2021~~ ground surface temperature data for the hydrological year 2020/21 to model bedrock surface temperatures time series from weather forcing on the period 1850 - 2022. Using a topographical downscaling method based on digital elevation model, we then create climatic boundary conditions for 1D and 2D heat transfer numerical simulations at the landscape level. In this way we obtain permafrost distribution maps and ad-hoc simulations for complex topographies. Our results are validated by comparison with temperature data from two lowland boreholes (100 m depth) and geophysical data describing ~~freezing~~frozen/~~unfreezing~~ unfrozen conditions across a mid-elevation mountain ridge. Finally, we use regional carbon pathway scenarios 2.6 and 8.5 to evaluate future evolution of ground temperatures ~~to 2100.~~ until the end of the 21st century. Our results indicate a sporadic permafrost distribution up to roughly 400 m.a.s.l., while future scenarios suggest a decline of deep frozen bodies up to 800 m.a.s.l., i.e. the highest summits in the area.

1 Introduction

~~Mountain permafrostis a typical cryospheric feature of~~ The term "permafrost" defines ground presenting temperatures that remain below 0 °C for at least two consecutive years. In cold mountain regions, ~~defined as perennially frozen ground occurring in complex topography . In the past decades, the scientific community focused on understanding the role of mountain permafrost in slope stability, in order to determine the rise of new natural hazards linked to the changing climate (Haeberli et al., 2010). Several studies proved a relationship between ground mechanical properties and permafrost characteristics, indicating that an~~

~~increase in rock temperature – involving increasing water content and decreasing ice content - generally causes a deterioration in mechanical stability. This deterioration consists of a decrease in compression and shear resistance (Davies et al., 2001; Yamamoto and Sp~~ ~~, as well as lower resistance to fracture initiation (Krautblatter et al., 2013), resulting in the breaking of rock bridges (Mamot et al., 2020) .~~

complex topography influences shading, snow distribution and ground type, causing a highly variable distribution of ground temperatures and permafrost (Etzelmüller, 2013). Several field studies describe a significant correlation between warming climate~~and an increase in~~ , mountain permafrost degradation and increased slope instability, observed as rockfall frequency (Ravanel and Deline, 2011; Gallach et al., 2020), large rockslide occurrence (Patton et al., 2019; Guerin et al., 2020; Frauenfelder et al., 2018; Walter et al., 2020), high elevation infrastructure destabilization (Duvillard et al., 2019) and debris permafrost creep rate increase (Marcer et al., 2021). ~~Overall, the scientific community agrees on the effects of climate change on slope instability in mountain permafrost~~ Therefore, understanding the spatial distribution of mountain permafrost and its future evolution is a key step in understanding these hazards, and several countries started comprehensive programs to monitor this phenomena as a basis for risk assessment (Pellet and Noetzli, 2020; Isaksen et al., 2022).

In Greenland, the scientific community still does not have a precise quantification of mountain permafrost distribution. Available models are based on numerical simulations at kilometer scale ~~, and either not calibrated , or calibrated using data representative~~ (Daanen et al., 2011), are not calibrated with in-situ data (Gruber, 2012), or valid for sedimentary terrain only (Obu et al., 2019). Furthermore, our understanding of the evolution of mountain permafrost in the region is limited, as only Daanen et al. (2011) investigates future permafrost distribution, although at 25 km resolution. ~~Indeed, permafrost temperature data from Greenland are limitedto few low-land boreholes that are not representative for higher elevation and complex terrain (Obu et al., 2019).~~ This knowledge gap challenges our understanding of mountain hazards and their evolution, preventing a ~~reliable~~ regional scale hazard assessment that Greenland urgently requires, as ~~most of the population resides in proximity of mountain areas. As a result, the scientific community does not have a clear idea about the role of permafrost warming in recent events, such as the landslide-triggered tsunami that tragically ravaged the settlement of Nugaatsiaq (Svennevig, 2019; Svennevig et al., 2020) or the debris flows that hit Siorapaluk (Walls et al., 2020).~~ landslides related to permafrost degradation are common (Svennevig, 2019; Svennevig et al., 2022, 2023; Walls et al., 2020) and the population is affected by these events (Strzelecki et al., 2020).

~~The first step to gather information on permafrost conditions in mountain terrain~~ A major challenge when modeling mountain permafrost in this region is due to data availability, as ground temperature data are limited to few low-land sedimentary boreholes that are not representative for higher elevation and complex terrain (Obu et al., 2019). A common strategy to overcome this issue is based on the ~~standard~~ approach developed in Switzerland in the early 2000's (Gruber et al., 2004) relying on a network of permanent surface temperature loggers. These data are ~~then~~ used for transient modelling of ground temperatures across 1D profiles in relation with depth (Westermann et al., 2016), ~~or~~ as well as in 2D (Magnin et al., 2017a) and ~~3D complex~~ more complex 3D geometries (Noetzli et al., 2007). Several studies model ground temperatures using numerical approaches, as TEBAL (Stocker-Mittaz et al., 2002; Gruber et al., 2004) and CryoGrid (Westermann et al., 2016; Czekirda et al., 2019; Gisnås et al., 2017; Myhra et al., 2017). Both models have a numerical approach to the evaluation of the Surface Energy Balance (SEB), i.e. the transfer from weather parameters to surface energy flux as upper boundary condition for the heat transfer module. Other studies have handled the SEB problem using an empirical approach based on correlating weather data and measured ~~Surface ground temperatures (Magnin et al., 2017a; Etzelmüller et al., 2022a; Rico et al., 2021; Legay et al., 2021). The advantage of this approach is that it does not require complex climatic inputwhich may not be always available, still reaching good performances.~~ ground surface temperatures (Magnin et al., 2017a; Etzelmüller et al., 2022b; Rico et al., 2021; Legay et al., 2021) . This approach has the advantage of reaching good performances while requiring only basic climatic input, i.e. air temperature and solar radiation.

~~Using this latter modeling approach, we aim to provide a first quantification of mountain permafrost conditions in Greenlandby focusing in~~ Another challenge in modeling mountain permafrost is due to the influence of snow cover. Snow is known to cause severe disturbance to ground surface temperatures, which can significantly affect active layer thickness even when accumulating in isolated patches (Magnin et al., 2017b). Models are sensitive to snow characteristics (Etzelmüller et al., 2022b) , causing estimation of permafrost extents to greatly vary depending on the modeling assumptions (Czekirda et al., 2019). Although some numerical models are able to describe snow physics at hectometric resolution (Gisnås et al., 2014), it becomes extremely challenging to achieve a good knowledge of spatial characteristics of the snow in complex terrain, given the spatial variability of weather forcing, as wind and shading. To overcome this issue when modeling mountain permafrost, snow is often accounted with a topographical approach, based on filtering snow covered areas using a slope threshold (Magnin et al., 2019) to exclude them form the model or to apply specific offsets (Etzelmüller et al., 2022b; Boeckli et al., 2012). Overall, this method allows for a first order quantification of ground temperatures in complex terrain when detailed snow data are not available.

The aim of this study is to move a first step towards a high resolution regional characterization of mountain permafrost in Greenland. To do so, we focus on the Sisimiut area, (68° N on the west coast)~~. Instead of accurate weather data, we dispose of a large number of Ground Surface Temperature (GST) measurements, as in~~ , where we have a relatively large amount of data. In fall 2020 we installed 28 surface temperature loggers in the area measuring Ground Surface Temperature (GST), covering the local range of elevations and aspects. Using these data, we train a statistical model to evaluate the correlation between weather variables and measured GST. Weather data are downscaled using a basic elevation-gradient and solar exposure approach based on a Digital Elevation Model. ~~Once the~~ The statistical model is ~~trained, we use it to predict~~ then used to compute time series of GST at ~~the landscape scale and longer temporal frames, allowing creating the~~ any location in the landscape and for the period 1850-2022. Snow influence is modelled using a probabilistic approach quantifying presence/absence of persistent snow cover, which tunes an empirical temperature offset added to the GST time series. These time series are used as boundary conditions for a heat transfer model. In this study, we use COMSOL Multiphysics® heat transfer module, connected to Matlab ~~using LiveLink~~ through LiveLink (COMSOL Inc., 2015). We test our model for 1D simulation, which we compare to temperature data obtained by two ~~100m~~ 100 m deep boreholes drilled in ~~the area~~ bedrock at low elevation in 2019 and 2021. To obtain field data on ground temperature at high elevation, we used the approach proposed by Duvillard et al. (2020) ~~consisting in~~ based on geophysical surveys and calibration of resistivity - temperature dependencies in laboratory experiments. This methodology ~~allows to obtain~~ develops a bidimensional transect of ground freezing conditions at a given survey date~~.~~ , which is compared to our 2D numerical simulations. Finally, we model future evolution of permafrost distribution in the area using scenarios

RCP 2.6 and RCP 8.5, observing a relevant permafrost loss. Overall, this study provides an insight on mountain permafrost distribution in central-West Greenland, highlighting how this system is sensitive to recent and future climate changes.

2 Study site

Our study site is located ~~around the West Greenland town of Sisimiut, which is located~~ in the mountains surrounding Sisimiut, a city on the coastline of the widest non-glaciated area in West Greenland, about 200 km from the Greenland Ice sheet (see ~~figure 1~~Fig.1). Sisimiut is the second largest city in Greenland, counting 5582 inhabitants in 2020 and experiencing a rapid development. The ~~landscape is characterized by narrow fjords, alpine summits and isolated coastal glaciers. The dominant lithology is amphibolitic gneiss (Ljungdahl, 1967). The mountains of the region typically have pyramid-shaped summits and steep rockwalls. The Sisimiut town is~~ city is surrounded by two main mountain ridges: the Nasaasaaq – Appillorsuaq ridge to the south, summiting at 784 m.a.s.l., and the Palasip Qaqqa– Sammisoq ridge to the ~~North~~north, summiting at 605 m.a.s.l.. The landscape is characterized by narrow fjords, alpine summits and isolated coastal glaciers. The dominant lithology is amphibolitic gneiss (Ljungdahl, 1967). The mountains of the region typically have pyramid-shaped summits and steep rockwalls generating debris slopes underneath. Mountains are dominated by bedrock, although vegetation patches are common at up to 400 m.a.s.l.

Climatically, Sisimiut is located in the low arctic oceanic area~~(Jensen 1999), with a mean annual temperature of -1.8 °C for the period 2000 - 2020 (Cappelen and Jensen, 2021) and mean annual total precipitation of 382 mm at sea level (Period 1961 – 1990)~~, and weather data are recorded at the airport weather station (Cappelen et al., 2021; Cappelen and Jensen, 2021). The warmest month is July (6.3 °C on average), while the coldest is March (-14.0 °C). Mean annual air temperature increased ~~by 2.2~~ from -3.5 °C ~~from the period 1980 – 2000 to the period 2000 – 2020, while precipitation remained substantially unchanged. This temperature increase~~ in 1961-1981 to -1.8 °C in 2000-2020. Mean annual precipitation decreased from 509 mm in 1961-1981 to 422 mm in 1984-2004, year in which the rain gauge was decommissioned. Decrease in precipitation concerns both solid (mean monthly precipitation in January-April decreased from 28 mm in 1961-1981 to 25 mm in 1984-2004) and liquid (mean monthly precipitation in June-September decreased from 58 mm in 1961-1981 to 49 mm in 1984-2004) precipitation. This climate locates Sisimiut in the sporadic permafrost zone (Obu et al., 2019; Biskaborn et al., 2019), and morphologically active rock glaciers are present in the area, reaching sea level elevation (see Fig.1a). The recent climatic change on the other hand is believed to have caused significant glacial retreat in the coastal glaciers in the area, which lost about a fourth of their volume in the past three decades (Marcer et al., 2017). ~~The coastal region around Sisimiut is situated in the sporadic permafrost zone (Obu et al., 2019; Biskaborn et al., 2019). In the area are observable some morphologically active rock glaciers reaching sea level elevation.~~

3 Methods

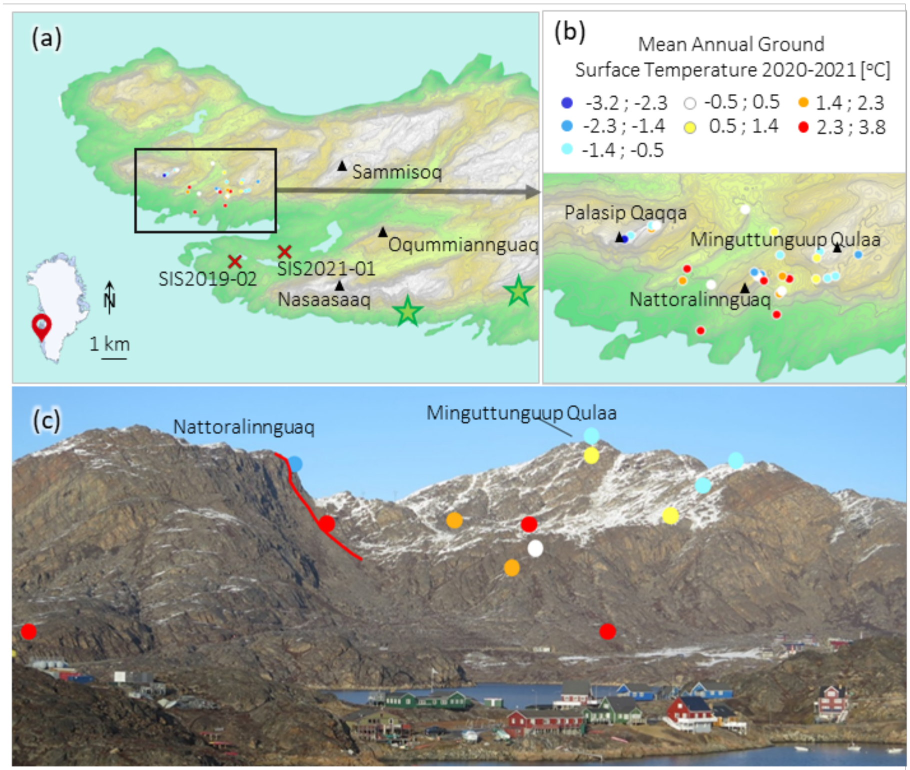

Figure 1. Study site summary. ~~In panel (a) is shown the map~~ Map of the entire study area (a), with location of deep boreholes SIS2019-02 and SIS2021-01 and rockglaciers fronts, identified by green stars. ~~On panel (b) is shown the detail~~ Detail of the Nattoralinnguaq area, where most of the ~~ground surface~~ GST sensors are installed ~~. On panel~~ (~~c~~b)~~is shown the south~~. South face of Nattoralinnguaq and Miguttunguup Qulaa (picture taken from Sisimiut in October 2020) with ~~surface~~ GST loggers ~~location~~ and ~~ERT location~~geophysical profile locations (c). Loggers are colored based on their measured mean annual surface ground temperature (fall 2020 to fall 2021). Elevation data belong to the Arctic DEM ~~(Porter, 2018)~~(Porter, 2018).

~~Our study is based on field data acquisition of ground temperatures , which are then used to calibrate a model, used to describe present and future permafrost conditions in~~

3.1 Ground temperature monitoring

Ground temperatures are monitored by a network of temperature sensors installed in various settings across the study area.

3.2 ~~Field data~~

3.1.1 ~~Ground temperature monitoring~~

~~As part of this study, we established a ground temperature monitoring network comprising both ground surface temperature (GST) monitoring and borehole temperature (BT) monitoring to a depth of 100 m.b.g.s.~~ All sensors used for the temperature data acquisition were custom zero-point calibrated using a Fluke 7320 compact bath with a manufacturer specified temperature stability and uniformity better than 0.01 °C. The bath temperature was measured using a Fluke PRT 5610 secondary standard temperature probe, and each sensor was immersed in the bath for 40 minutes while logging every 30 seconds. After the sensor temperature stabilized, the sensor offset was calculated as $\Delta T = (\sum_{(i=1)}^{n}[T_{ref,i} - T_{s,i}])/n$, where $T_{s,i}$ [°C] is the i^{th} sensor temperature measurement in the calibration period, $T_{ref,i}$ [°C] is the corresponding bath temperature measured by the PRT sensor at the same time, and ΔT [°C] is the average calculated sensor offset, which was applied as a correction to each field temperature measurement collected by that sensor. ~~The total combined uncertainty of the calibration bath reference temperature is better than 0.02 °C (k=2).~~

3.1.1 ~~Ground Surface Temperature~~

We established a GST monitoring network consisting of 28 individual monitoring locations, covering as evenly as possible the range of aspects, elevations and slopes at the study site~~, and data~~. Data were acquired for one year, from fall 2020 to fall 2021. The technical information about loggers used are summarized in ~~table 1. Both DS1922L and M5-Rock are sensors~~ Table 1. Both iButtons and Geoprecisions are widely used in permafrost studies and the community has previous experience in their strength and weaknesses ~~(Gruber et al., 2004; Gubler et al., 2011)~~(Gruber et al., 2004; Gubler et al., 2011; Magnin et al., 2015a, 2019; Hipp et al.,

. This combination of loggers is ~~common as a~~ a common trade-off between equipment costs and data quantity/quality. The ~~DS1922L~~ iButtons are low-cost digital chip temperature sensors, which provide a reasonable temperature resolution of 0.0625°C. ~~However~~Our calibration show that iButtons have offsets reaching a maximum of 0.7 °C. Additionally, since they are primarily designed for indoor use, they are prone to failure when used in harsh environment~~and~~. According to Gubler et al. (2011), about 5-10% of the deployed loggers can be expected to fail ~~(Gubler et al., 2011). Protecting~~ and protecting the logger with plastic film (as we did) helps to reduce failures. ~~The M5-Rock~~ Geoprecisions on the other hand are more expensive and reliable loggers, which provide a better quality measure. ~~Geoprecision~~ According to our calibration, Geoprecision offsets reach a maximum of 0.10 °C. Finally, Geoprecision loggers can be accessed ~~by radio, allowing remote~~ remotely, allowing download of data ~~(~~within 10-20 m range~~)~~, which becomes handy in steep terrain.

Given these characteristics, we decided to install nine ~~M5-Rock~~ Geoprecision loggers in steep bedrock, as these data are strategically more relevant in the context of the study. These loggers were placed by drilling a 10 x 300 mm hole and sealing the sensor using frost resistant resin. For The iButtons (~~28~~ 19 loggers in total), were installed in other more accessible conditions, such as flat bedrock (~~13~~6), soil (11) and easy-access rockwalls (~~4~~2) (See ~~figure 1).~~ Fig. 1). In bedrock conditions, loggers were placed in 22 x 100 mm holes, sealed with a mixture of sand and frost resistant sealant. In soil conditions, loggers where placed in 50 mm holes manually dug in gravel.

	GST			Deep Boreholes	
Nb	19	5	4	1	1
Brand	Maxim integrated	Geoprecision	Geoprecision	Geoprecision	HOBO
Type	iButton	MLog5W Rock	MLog5W STRING	MLog5W STRING	5-inch Probe
Sensor	DS1922L	PT1000	Tnode	Tnode	U12-015-02
Resolution [C]	0.063	0.001	0.01	0.01	0.03
Accuracy [C]	0.5	0.1	0.1	0.1	0.25
Logging interval [hr]	4	1	1	1	0.00028
Sensor(s) depth [m]	0.05	0.3	0.3, 0.9	[0.1,0.5,1.0,1.5,2.0,3.0, 4.0,5.0,7.5,10.0,12.5,15.0, 17.5,20.0,25.0,30.0,35.0,40.0, 45.0,50.0,55.0,60.0,65.0,70.0, 75.0,80.0,90.0,99.0]	[1,5,10,15,20,25, 30,35,40,45,50,55, 60,65,70,75,80,85, 90,95,97.5]
Terrain	Soil, Bedrock, Steep Bedrock	Steep bedrock	Steep bedrock	SIS2021-01	SIS2019-02

Table 1. Summary of sensors and their specifications used to measure GST in the study area form fall 2020 to fall 2021.

3.1.1 ~~Deep Ground Temperature~~

Two 100 m deep boreholes, SIS2019-02 and SIS2021-01, ~~were~~ are drilled in bedrock outcrops in relatively flat terrain at 50 and 70 m.a.s.l. (see ~~Figure 1) . The boreholes were~~ Fig.1) and similar conditions of exposure to solar radiation, while snow conditions are different. SIS2019-01 is located in a drift accumulation area and the snow depth can reach 2 m, while SIS2021-01 is on a wind-exposed hill, which ensures snow-free conditions most of the winter. Both boreholes are drilled using a Sandvik DE130 compact core drill owned and operated by the Greenland School of Minerals and Petroleum, with wireline NQ drilling tools (outer diameter: 70 mm). The holes ~~were~~ are installed with a 100 m long PE casing (outer diameter 32 mm, inner diameter 26 mm), closed at the bottom with a heavy duty heat shrink end cap with heat activated glue. Borehole SIS2019-02 ~~is logged manually~~ does not have a permanent sensor installed, and it was logged manually three times since it was drilled. The measurement is done at 2 m depth intervals, using a HOBO U12-015-02 logger~~(zero-point calibrated in a triple-point of water cell)~~. The logger uses a 10 sec sampling interval and rests at each depth for two minutes. In the post processing, temperatures are averaged only over the last minute to obtain the temperature at a particular depth, thereby ensuring the sensor has equilibrated to the new temperature. The borehole SIS2021-01 is equipped with a permanent GeoPrecision thermistor string with 28 sensors (TNode, digital chip with 0.01 °C resolution). The upper-most sensor is located at 0.1 m.b.g.s., the lower-most at 99 m m.b.g.s. The sensor spacing progressively increases with depth from 0.4 m in the top to 10 m at depth, and the logging interval is 1 hr. ~~The two boreholes are drilled in similar conditions of elevation and exposure to solar radiation,~~

~~while snow conditions are different. SIS2019-01 is located in a drift accumulation area and the snow depth can reach 2 m, while SIS2021-01 is on a wind-exposed hill, which ensures snow-free conditions most of the winter.~~

3.1.1 ~~Geophysical profiles~~

~~The geophysical investigations were conducted on~~

3.2 Geophysical data

We measured a geophysical profile to obtain information on deep permafrost distribution in different topographical settings than the terrain hosting the two boreholes. The profile was conducted across the north and south faces of Nattoralinnguaq (353 m.a.s.l). ~~The summit presents~~ This summit presents typical characteristics of the mountains in the Palasip Qaqqa– Sammisoq ridge: a steep and rocky ~~South face about~~ south face approximately 100 m high with a debris slope underneath, and a more gentle ~~North~~ north face characterized by small vegetation patches and some short steeper sections. This ~~summit was chosen due to its proximity to town infrastructures, as well as for easy accessibility thanks to a~~ specific mountain was chosen for its accessibility, as the road leading to the airport passes just nearby a short path that leads to a popular viewpoint ~~at~~ to the summit.

~~The geophysical~~ Electrical resistivity tomography (ERT) yields only qualitative information on the thermal state of materials because electrical conductivity depends on many parameters including water content, salinity, cation exchange capacity, and temperature. The advantages of these geophysical methods are their low cost and the fact that they provide 2D or 3D tomograms/images of the subsurface. The geophysical investigations were conducted in early October 2020 using Electrical Resistivity Tomography. Five ~~100-m-long cables (500-m-long~~ 100 m long cables (500 m long profile) and a total of 100 electrodes (~~5-m-spacing~~deployed with 5 m spacing) were connected to a resistivity meter (~~GuidelineGeo~~ Guideline Geo Terrameter LS2 powered by a 12 V external battery). We used 10 mm x 100 mm stainless steel electrodes, inserted in pre-drilled holes with a paste of salty bentonite to improve ~~electrical grounding~~ the galvanic contact/reduce the contact resistances and prevent freezing (Krautblatter and Hauck, 2007; Magnin et al., 2015b). The Wenner configuration was used because of its best signal-to-noise ratio in complex environments ~~due to its particular electrode configuration since the voltage electrodes MN are located in-between the current electrodes AB~~ (Dahlin and Zhou, 2004; Kneisel, 2006). Topography ~~along the profile was obtained thanks to a handheld GPS and altitude were obtained using a metric~~ was extracted from a 2 m resolution digital elevation model (DEM~~).~~

~~We cleaned 28~~, Porter (2018)) based on electrode positions measured with a handheld GPS device. We cleaned 4% of the data point acquired before the inversion (~~734~~ 549 points acquired, 528 inverted) ~~base and the standard deviation and~~ by filtering out the outliers from the pseudo section. The data were inverted with the RES2DINV-4.8.10 software using a smoothness-constrained least-squares method and the standard Gauss–Newton method (Loke and Barker, 1996). The inversion was stopped at the third iteration when the convergence criterion was reached.

3.2.1 ~~Laboratory experiences and temperature analysis~~

In addition to the field measurements, we performed a laboratory electrical conductivity experiment on two ~~a rock sample~~ rock samples collected in the field from ~~an outcrop of the rockface and the middle of the south~~ the rockwalls on the south and north face. ~~Three~~ These analyses define the relation between resistivity collected in the field and freeze-thaw conditions of the ERT transect. The three granite cubic core samples considered for laboratory analyses (sample G-RF, G-LR and G-DA) ~~was~~ are characterized by a porosity of Φ = ~~0.046~~ 0.032 for G-RF, Φ = ~~0.032~~ 0.015 for G-LR and Φ = ~~0.012~~ 0.023 for G-DA. Before performing the laboratory measurements, the samples ~~was dried during~~ were dried for 24 ~~hr~~ hours at 60 °C, then saturated under vacuum with degassed water from melted snow taken in the field. The samples ~~was~~ were then left several weeks in the solution to reach chemical equilibrium~~before performing the laboratory measurements~~. The water conductivity at 25 °C and at equilibrium was ~~9.56 10-3 Sm~~0.0118 S m^{-1} for ~~G-RF and 1,157 10-3 Sm~~G-DA and 0.0142 S m^{-1} for ~~G-LR and G-DA~~G-RF and G-LR. The sample holder was placed in a heat-resistant insulating bag ~~and placed in a freezer for seven days at -22~~immersed in a thermostat bath (KISS K6 from Huber; bath volume: 4.5 l). The temperature of this bath was controlled with internal sensor the temperature of the sample was control with external sensor with a precision of 0.1 °C. ~~Measurements were then made during the temperature rise~~Glycol was used as heat carrying fluid and the conductivity measurements were carried out with the impedancemeter. The (in-phase) conductivity measurements shown here are obtain at a frequency of 1 Hz. We moved the freezing point temperature T_F = 0 °C based on direct observations on instrumented boreholes for G-RF. The measurements with T_F = ~~2~~ -3 °C reflect the fact that the measurements were made only in the ~~upward~~ downward direction of the temperatures and not in the ~~downward~~ upward direction. These analyses define the relation between resistivity collected in the field and freeze-thaw conditions of the ERT transect.

3.3 Modeling

Our modeling approach is based on a mixed statistical-numerical methodology, which is conceptually similar to the study developed by Magnin et al. (2017a) and the modelling section in ~~Etzelmüller et al. (2022a)~~Etzelmüller et al. (2022b). The methodology ~~consists in evaluating~~ evaluates Ground Surface Temperature (GST) time series with an empirical approach, which are then used as upper boundary conditions for a heat transfer numerical model. This modelling methodology ~~can be divided in a three-steps~~ refers to a four-steps workflow: (i) acquisition of climatic forcing data and downscaling, (ii) statistical modeling and prediction of GST data~~and~~ , (iii) snow cover modeling and (iv) numerical modeling of heat transfer in bedrock.

3.3.1 Forcing data and downscaling

The weather ~~input~~ data were retrieved form different sources covering different periods - summarized in ~~table 2. Concerning datasets a and b, since only data from~~ Table 2. Weather station data for Sisimiut are available only starting in 1958, while weather stations have been running in Nuuk (300 km ~~South~~south) and Ilulissat (250 km ~~North) are available~~ north) since 1784. Therefore, we generated a custom dataset for Sisimiut covering the period prior to 1958 (dataset a). For air temperature, we evaluated the regression between ~~datasets a and b~~ data from Nuuk and Ilulissat (datasets e1, e2) over the overlap period

Dataset reference	Label	Period Available	Period used	Variables	Data type	Location
Custom made	a	1784-2021	1850-1979	Air tempertaure Solar radiation	Interpolation from e1, e2 and e3* Extrapolated from dataset b	Sisimiut
Herbasch et al 2019	b	1979-present	1979-2022	Air temperature, solar radiation, cloud cover, dew point, wind speed/direction, precipitation	Reanalysis	Global 0.5 degs
Hofer et al 2020, RCP 2.6	c	2006-2100	2022-2100	Air temperature, solar radiation	CMIP model	Global 0.5 degs
Hofer et al 2020, RCP 8.5	d	2006-2100	2022-2100	Air temperature, solar radiation	CMIP model	Global 0.5 degs
***Used to generate air temperature of dataset a**						
Cappelen et 2021a	e1	1784-2021		Air temperature	Weather station	Nuuk
Cappelen et 2021a	e2	1784-2021		Air temperature	Weather station	Ilulissat
Cappelen et 2021b	e3	1958-2021		Air temperature	Weather station	Sisimiut

Table 2. Summary of climatic databases used to cover the investigation period (1850 -2100). Datasets a and b are used for modelling present day ground temperatures. Datasets c and d are used for simulating scenarios RCP 2.6 and RCP 8.5 respectively. Datasets e1, e2 and e3 are used to model air temperature in Sisimiut for dataset a, as long term weather station data are not available at this location.

~~1958-2020~~1958-2022 with weather data from Sisimiut (dataset e3). The regression ~~predicts air temperature in Sisimiut using dataset a~~ is then used to generate air temperature for the period ~~1850-1958, creating air temperature for dataset c. Since datasets a and b~~ prior to 1958. For solar radiation, weather stations in Nuuk, Ilulissat and Sisimiut did not have ~~measurement of solar radiation, we assigned them~~ this variable measured. We generated a synthetic estimation equal to the average year over the period 1979-2022 ~~(dataset d). Dataset dwas downloaded by~~ retrieved from global reanalysis model (dataset b). The other datasets, b to d, are publicly available and ready to use. Dataset b was downloaded from the Copernicus database (Hersbach et al., 2020), and we selected the standard set of predictor variables used by CryoGrid SEB module ~~. In order to understand future evolution of permafrost in the area, we simulated future GST forced by the Norwegian Erath~~ (Westermann et al., 2016). For future scenarios, we used the Norwegian Earth System Model version 1 (NorESM1) global circulation model, using Representative Concertation Pathway (RCP) 2.6, and RCP 8.5 for 2006-2100 (Bentsen et al., 2013). ~~We chose the~~ The NorESM1 model ~~as~~ is also chosen by several authors in Greenland for cryosphere evolution modelling due to its good performance in the region (Colgan et al., 2016; Hofer et al., 2020) thanks to his good performance in the region (Fettweis et al., 2011). The RCP 2.6 is the NoreESM1 outcomes for scenarios of declining emissions since 2020 (optimistic scenario, dataset ~~e~~c), while the RCP 8.5 is simulated with unregulated emissions increasing at a rate compatible to the present-day industrial development (pessimistic scenario, dataset ~~f~~d).

Air temperature and solar radiation are downscaled at any location in our study area using a topographical approach. The downscaling ~~was dependent on three~~ depends on two parameters: elevation ~~,~~ and potential incoming solar radiation (PISR)~~and snow cover probability~~. Elevation is used to downscale air temperature by applying a constant lapse rate of ~~0.47~~0.047 °C ~~/100~~ ~~m~~m^{-1}, measured on the study area by the ~~MAGST~~ Mean Annual Ground Surface Temperature (MAGST) monitoring network by detrending the data for slope aspect and snow cover. The elevation data are obtained ~~by the Arctic digital elevation model (DEM) at 10m~~ from the Arctic DEM at 10 m resolution (Porter, 2018). ~~PISR is used to downscale the solar radiation forcing~~

~~by~~ Solar radiation forcing is downscaled using the ratio between ~~Potential Incoming Solar Radiation at the~~ the PISR at each logger location and the PISR at the ERA5 reference ~~cell~~grid. The PISR map is evaluated using ~~SAGA by applying the PISR module to the DEM~~ the software System for Automated Geoscientific Analyses (SAGA) and the module PISR (Conrad et al., 2015).

~~Snow influence is evaluated not by directly downscaling a forcing parameter, but rather the GST timeseries resulting from the GST model (see next section). This is done by applying a constant offset: $GSTs_i(z_i, PISR_i) = GST_i(z_i, PISR_i) + dTs * SnowP_i$; where GST_i is the GST depending on~~

3.3.2 GST Modeling

In this step, we model the relationship between forcing and GST data using a data-driven approach. Here, we use snow-free GST data, as snow cover effects will be modelled in the next step. Previous studies used an offset-based approach based on the evaluation of a constant thermal offset between air temperature and snow free GST (Magnin et al., 2017a; Etzelmüller et al., 2022b) . In our study, we use a conceptually identical approach, based on the following hypothesis (Magnin et al., 2019): the ~~local elevation z and PISR, used to downscale~~ snow-free GST can be predicted by an empirical model trained using available forcing variables that dominate GST distribution on steep bedrock. To do so, we aggregate each snow-free GST measurement to the forcing data that occurred during that acquisition time step, downscaled at the logger location. While GST data from the period 2020-2021 are used as dependent variable, the climatic datasets overlapping on the same periods are used as predictors. Datasets a, c and d (see Table 2) are fitted to the GST data using air temperature and solar radiation ~~. dTs is the thermal offset due to~~ as predictors. For dataset b, we also use cloud cover, dew point temperature, total precipitation, wind speed and direction as additional predictors. This creates a database of Nx1 targets and NxM data points, where N is the number of available GST data and M is the number of climatic predictors used. We then split this database into training and validation sets, following a pseudo-randomized cross validation approach, as we randomly exclude entire GST time series from training. We choose a multinomial linear model, trained with the Matlab function fitlm.

3.3.3 Snow cover modeling

In order to model snow cover, ~~which we evaluated~~ we develop a methodology based on constant offset similar to Etzelmüller et al. (2022b) . We first evaluate the average temperature offset due to snow cover by comparing the mean annual GST of sensors that were/were not snow covered during the entire winter 2020-2021. ~~SnowPi is~~ This offset then is multiplied to the local probability of snow cover presence/absence, that we call SnowP, varying from zero (absence of snow cover) to 1 (presence of long lasting snow cover). We ~~created the SnowP map~~ compute the SnowP by training a neural network classifier with a categorical variable describing presence/absence of snow at specific locations, and topographical data describing slope angle and curvature (planar, longitudinal and profile - obtained with the morphometric features module in SAGA, Wood (2009)) at those locations. This dataset is created by interpretation of ~~landscape pictures taken during winter in~~ 5 landscape pictures of the study area ~~and assigning~~ taken at the peak of the snow accumulation season (late April) in winters 2021 and 2022. We manually assigned snow/no snow areas ~~on a GIS~~ in a GIS and combined this dataset to terrain parameters to train a binary classifier. The classifier provides a probability of snow cover for a given set of curvature and slope, which can be extrapolated at the landscape scale creating a map of snow cover probability SnowP (~~figure 2).~~

~~Comparison of the SnowP map (3D visualization) with a field picture of the North face of Nasaasaaq taken in May 2021 from the summit of Oqummiannguaq. The SnowP map correctly identifies snow free steep terrain (1), steep chutes that are mostly snow covered (2) and gentle terrain snow free because of wind erosion (3).~~

3.3.4 ~~Statistical modeling of GST~~

~~In this step, we model the relationship between forcing and GST data using a data-driven approach. Previous studies used an offset-based approach based on the evaluation of a constant thermal offset between air temperature and GST (Magnin et al., 2017a; Etzelmü~~ ~~. In our study, we use a conceptually identical approach,~~ Fig.2). The map identifies drift traps where snow is most likely to accumulate. The validity of this method is based on the ~~following hypothesis: the GST can be predicted by an empirical model trained using available forcing variables that dominate GST distribution on steep bedrock (air temperature, solar radiation, wind characteristics, precipitation and humidity for dataset d, and air temperature and solar radiation for datasets c, e and f). To do so, we aggregate each GST measurement to the forcing data that occurred during that acquisition time step, downscaled at the logger location. This creates a database of Nx1 targets and NxM predictors, where N is the number of available GST data and M is the number of climatic predictors used. We then split this database into training and validation sets, following a pseudo-randomized cross validation approach, as we randomly exclude entire loggers time series from training. This allows observe the model's performance in predicting GST at locations not used in the training process. We use a multinomial linear model, trained using the Matlab function fitlm. Since all datasets cover the period 2020-2021, i.e. when we have our GST measurements, this process is done to cover the whole period 1850 - 2100, creating four independent models, each trained on a specific dataset.~~ observation that snow drift patterns in the arctic are generally stable over time due to relatively dry and windy weather (Parr et al., 2020).

3.3.4 Numerical modeling of heat transfer

Heat transfer is simulated in 1D conditions for model calibration and large scale mapping, while 2D simulations are restricted to areas of interest for more detailed analysis. The heat transfer process is modelled using the "heat transfer in porous media" module in COMSOL, which assumes ~~valid~~ the local thermal equilibrium hypothesis to be valid. The model accounts for three materials: solid matrix, fluid and solid with phase change~~– all materials parameters are summarized in table 3.~~ . The fluid phase is the default COMSOL "water" material, to which we assigned a phase change to ice at 273.15 K and transition interval to ice of ~~5K~~5 K, according to Noetzli and Gruber (2009). ~~The~~ Since we do not have precise information on ground thermal properties, the porous matrix material is assigned as the default ~~material~~ crystalline rock "granite" K = 2.9 ~~W(m*K)~~$\mathrm{Wm^{-1}K^{-1}}$ and Cp = 850 ~~J(kg*K)~~$\mathrm{Jkg^{-1}}$~~.~~ $\mathrm{K^{-1}}$. A quick sensitive analysis shows that the model computes ground temperature differences smaller than 0.01 °C when varying these parameters within the typical ranges of different crystalline rocks. For the 1D model we entered a custom function to describe the matrix density, which was evaluated from the cores extracted ~~form~~ from SIS2021-01, providing an empirical function of depth increasing from 2600 $\mathrm{kgm^{-3}}$ ~~in the subsurface~~ at the surface to 3000 $\mathrm{kgm^{-3}}$ at 20 m

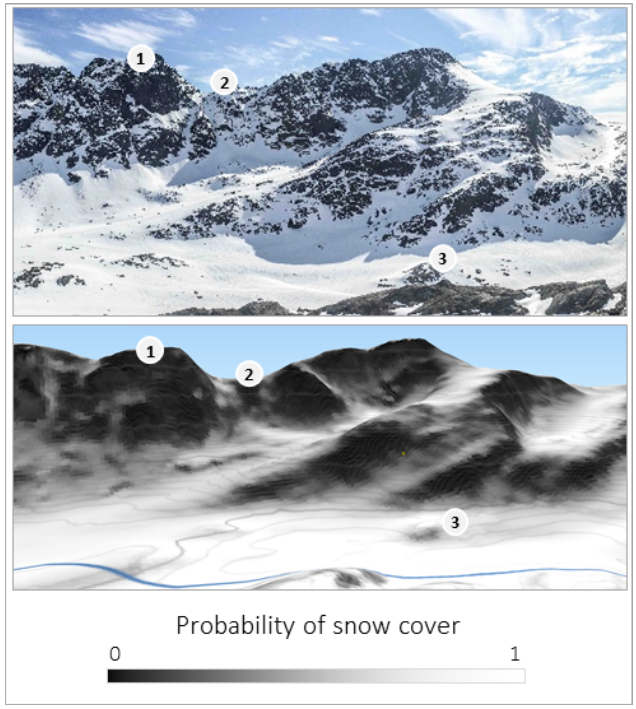

Figure 2. Comparison of a field picture of the north face of Nasaasaaq (a) taken in May 2021 from the summit of Oqummiannguaq and the SnowP map (b, 3D visualization). The SnowP map identifies snow free steep terrain (1), steep chutes, drift traps, that are mostly snow covered (2) and gentle terrain features that are snow free because of snow drift (3).

depth, and being constant until 100 m depth. We attributed the ~~average~~ constant density of 3000 kgm^{-3} to the 2D models, as it not known if the near-surface values measured at SIS2021-01 are representative for the entire study area.

The numerical simulation consists of four successive studies: a stationary study for initial conditions (mean conditions for 1850-1860, forcing dataset ~~c~~a), a transient study 1850-1979 (~~dataset c~~forcing dataset a), a transient study 1979-2022 (forcing dataset ~~d~~b) and a transient study 2022-2100, depending on the scenario chosen (RCP 2.6 and RCP 8.5 - forcing datasets ~~e,f~~c,d). For each time period (1850-1979; 1979-2022 and 2022-2100), the corresponding GST model and forcing time series are stored in COMSOL as analytical functions using local elevation, PISR, SnowP and time as parameters that can be modified by the user to reproduce ground temperatures in different topographical settings. Therefore, by entering custom local topographical conditions, the ~~COMSOL~~ GST model will produce downscaled GST time series ~~and use them~~ that are imposed as upper boundary conditions for the COMSOL heat transfer module. As lower boundary condition, we ~~used~~ impose the constant geothermal heat flux, which we also evaluated from the SIS2021-01 data. Our data indicate a temperature gradient of 0.015 °~~Cm~~C m^{-1}, which, considering a thermal conductivity of 2.9 ~~W(m*K)~~Wm^{-1}K^{-1}, gives a constant geothermal heat flux of 0.045 Wm^{-2}.

3.3.5 Model calibration

The numerical model ~~was~~ is calibrated for two parameters: matrix porosity and initial conditions in 1850. The calibration ~~was carried~~ is carried out by simulating conditions in SIS2021-01, ~~which was modelled~~ from 1850 to 2022 using a 1D geometry of a ~~100m column. Both parameters are calibrated carrying the simulation from 1850 to 2022 and comparing model results to data available from SIS2021-01, i.e. from~~ 100 m column. The simulation results are then compared to the field data acquired during the period August 2021 to April 2022. ~~We evaluated the~~ This is repeated for different combinations of matrix porosity and initial conditions, aiming to minimize the difference between data and model results. For boundary conditions, we evaluate the GST at the location of SIS2021-01 using the downscaled climatic variables over the period 1850-2022. For downscaling, we ~~evaluated~~ evaluate elevation, PISR and snow cover probability on the respective raster maps (elevation = 77 ~~masl~~m.a.s.l., PISR = 790 $kWhm^{-2}$, SnowP = 0.3). We ~~tested~~ test different porosity values according to previous studies findings and field measurements, i.e. porosity ranging from 0.01 (Rico et al., 2021) to 0.05 (Magnin et al., 2017a). As initial conditions, we ~~evaluated~~ compute the temperature profile of the stationary solution of the 1D model forced by the average GST over the period ~~1850-1860. We then added~~ 1850 - 1860. We then add a positive ground temperature offset as parameter to account the fact that temperatures in 1850 – 1860 (at the Little Ice Age peak) were lower than the previous period, and deep ground temperatures were likely higher than ~~what~~ modelled by our stationary model . The optimization of the two parameters ~~targeted~~ targets the best fit between measured and modelled ~~deep ground temperatures (below 20m depth), as well as active layer thickness~~temperatures below the depth of zero annual amplitude.

3.3.6 Mapping ground temperatures

The ground temperature map ~~was~~ is computed by evaluating the calibrated 1D model for each set of topographical condition in our study area. This process is handled by Matlab's Livelink, which runs the routine through each gridcell in the DEM, PISR and SnowP maps, and passes the local topographical parameters to the 1D COMSOL model. The COMSOL studies are run ~~from~~ through Matlab command and the export is stored in a text file which contains the evolution of temperature in the ~~column~~ 1D model over time for each ~~study. Matlab then~~ gridcell. Considering that the depth of zero annual amplitude measured at the borehole locations is approximately 10-20 m, we compute the mean ground temperature (2012-2022) at 20 meters depth (MGT20) as a proxy for mapping permafrost presence. Matlab imports the output at each loops and stores the ~~Mean Ground Temperature at 20m depth in the period 2012-2022 (~~MGT20 ~~)~~ and assigns it to the corresponding raster cell, creating the MGT20 map.

3.3.7 2D Models

The ~~2D model computed for the ERT location and~~ use of a 1D model for the ~~Nasaasaaq summit~~mapping module disregards lateral influences, and we expect our map to be imprecise in the proximity of sharp slope breaks and ridges. 2D models on the other hand provide a much stronger approximation in complex terrain, as they ~~present complex topography. Both areas have interests as we would like~~ provide similar results for 3D transient simulations (Noetzli et al., 2007). For this reason, we compute 2D model for two location of special interest: the ERT profile and the Nasaasaaq summit. The first location is chosen to compare the ERT data to our model, ~~as well as observing permafrost evolution at Nasaasaaq -~~ while the second location allows us to model and understand permafrost distribution and evolution in the tallest mountain in the study area. For each location we ~~imported the elevation profile z in COMSOL and converted to a solid~~ set-up a north-south transect in the QGIS software, and used it to sample the elevation profile from the DEM. The elevation profiles are then imported into COMSOL as 2D geometry using the parametric function option. ~~Also~~ The same method is used to import PISR and SnowP ~~are imported as interpolation functions whose coordinates are consistent to the reference system of the solid representing the terrain~~along the transects. In this way, we can provide the GST model as an interpolation function over the spatial variable (x) and temporal variable (t): ~~$GST(x,t) = f(z(x), PISR(x), t) + dT * SnowP(x)$, being f~~ $GST(x,t) = f(z(x), PISR(x), t) + dT \cdot SnowP(x)$, where f is the linear GST models for each forcing dataset. As lower boundary condition, we ~~used~~ impose the geothermal heat flux of 0.045 $\mathrm{Wm^{-2}}$ evaluated ~~form~~ from the borehole SIS2021-01, while we ~~implemented~~ impose zero-flux conditions on the lateral boundaries.

4 Results

4.1 ~~Sensors calibration~~Ground temperature monitoring

~~he sensors calibration revealed that DS1922-L have an average absolute temperature offset of 0.20°C, reaching a maximum of 0.71°C. The standard deviation of the measurement is 0.02°C. M5-Rock offsets are on average 0.04°C, reaching a maximum of 0.10°C, while the standard deviation of the measurement is below 0.01°C. Sensors' offsets are applied as correction to each corresponding logger measurements.~~

4.2 ~~Measured ground temperatures~~

4.2 ~~Boreholes~~

~~Both boreholes show deep ground temperatures close to 0°C. SIS2019-02 was measured three times since its installations and presents an active layer of about 10m, and a minimum of temperature of +0.3°C at 30m depth, reaching +1.0°C at 100 m. SIS2021-01 has too short record to define precisely active layer depth, which seems to be around 10 m deep for summer 2021. Below 10m depth, ground temperatures are lower than SIS2019-02, reaching -0.2°C at 30 m and +0.3°C at 100 m. This indicates the presence of permafrost, which reaches 70 m depth.~~

4.1.1 ~~Ground surface temperatures~~

~~All loggers here reported run for one full year, from fall 2020 to fall 2021. Among the 27 loggers, fifteen presented snow free data~~ GST data are measured during one full year, as loggers were installed in September-October 2020, and retrieved one year later. Most loggers show sub-zero GST between early October and late May. Fifteen loggers present snow-free GST data (Fig. 3a), seven present thick snow cover and six present intermediate characteristics (Fig~~3). Concerning snow free loggers,~~

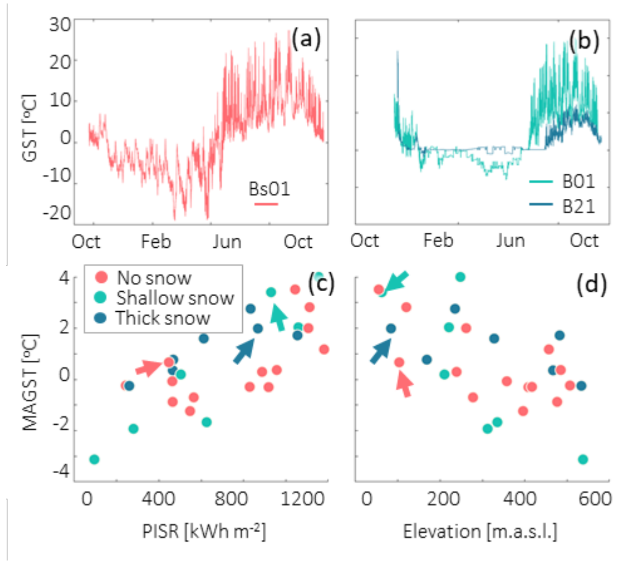

Figure 3. Summary of GST recorded by the loggers during 2020-2021. On top, examples of GST time series are for a snow free logger (a) and snow covered logger (b). On bottom, the MAGST in relation to topographical predictors Elevation (c) and Potential Incoming Solar Radiation (d).

~~the data show~~ . 3b). In general, snow cover onsets in early November and lasts until mid-June, although this depends on the specific logger location. Lowest GSTs are reached in late March, when several loggers recorded temperatures around -20 °C (see Fig. 3a). The lowest GST (-22.8 °C) is recorded on March 28 by a logger installed on a north facing bedrock slope at 476 m.a.s.l.. Highest GSTs are reached at the end July, as several loggers recorded temperatures above 25 °C. The data show that mean annual ground surface temperature (MAGST) ~~varying from +3.5 °C for south facing rockwall~~ is correlated with elevation and aspect (see Fig. 3c and d). To show the effect of elevation, we compare two snow-free loggers installed on south facing rockwalls, one at sea level ~~to~~ (MAGST = +~~1.2 C~~3.5 °C) and at 460 ~~masl.Aspect causes aMAGST~~ m.a.s.l. (MAGST = +1.2 °C). By comparing loggers installed on rockwalls at the same elevation but on opposite aspects, we obtain a MAGST offset of 2.2 °C from north ~~faces to south faces at similar elevations. When snow covers the loggers, these quantifications do not hold. On average, based on our data , the presence of snow cover causes an offset on the MAGST~~ to south facing slopes.

Boreholes temperatures are shown in Fig. 4. In SIS2019-02, the depth of zero annual amplitude is approximately 20 m. Below this depth, temperature data indicate a minimum of temperature of +~~1.58~~ 0.3 °C~~± 0.41~~ , reached at 30 m depth, and a temperature of +1.0 °C ~~when other conditions do not change (R^2 = 0.81). This value - +1.58~~ at 100 m. Since temperatures are positive below the depth of zero annual amplitude, the measurements at SIS2019-02 indicate absence of permafrost. SIS2021-01 shows consistently negative temperatures between 20 and 70 m depth, reaching a minimum of -0.2 °~~C- was assigned to dTs for GST downscaling.~~ C at 30 m depth. The depth of zero annual amplitude is approximately 10 m.b.g.s.. Since we measure negative temperatures below this depth, the data from SIS2021-01 indicate the presence of permafrost.

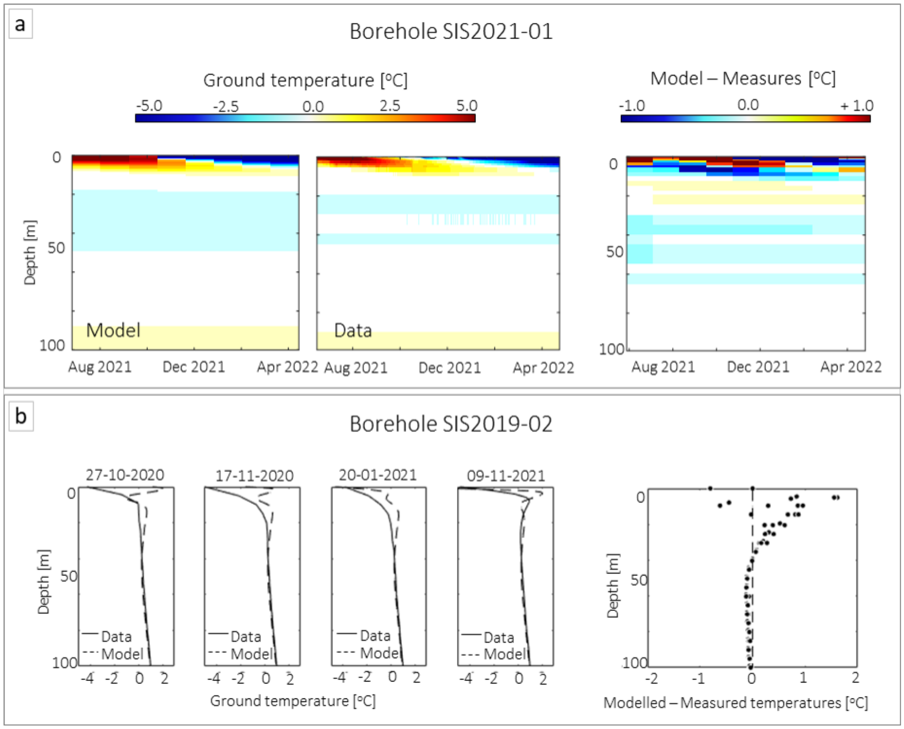

Figure 4. Data and model comparison for boreholes SIS2021-01 (a) and SIS2019-02 (b). For borehole SIS2021-01, data are acquired with an interval of 1 hr using a MLog5W-STRING, allowing us to color plot temperatures as function of depth and time. Data are compared to model results - see section 4.3.2. For borehole SIS2019-02, data were measured on four separate dates, using a5-inch Probe lowered manually into the borehole. These measurements produce four temperature profiles, i.e. temperature as function of depth, that are compared to the model results.

4.2 Geophysical survey

~~Electrical~~ As shown in Fig.5b, the electrical conductivity tomograms acquired show a vertical and also lateral variations distribution of the conductivities with ~~rather~~ low conductivity values (< $10^{-3.5}$ Sm^{-1}) below the ~~N and S face and higher~~ north and south face and high values inside the mountain (> $10^{-4.4}$ Sm^{-1}~~, Fig 5~~). The petrophysical analysis~~suggests a~~, shown in Fig.5a, highlights a transition zone from frozen to thawed conditions between $10^{-4.4}$ and $10^{\cancel{3,5}\,-3.5}$ Sm^{-1}. This ~~suggests~~ indicates that permafrost presence is restricted inside the mountain and ~~possibly closed~~ close to the surface in the ~~North face and lower~~ north face and the upper part of the ~~South face. The electrical conductivity anomaly on~~ south face. A large portion of the north face ~~occurs near alarge lithological fault that has an impact on the distribution of permafrost and ground characteristics~~appears unfrozen below 300 m.a.s.l., occurring at the same location of a lithological fault observable on the field.

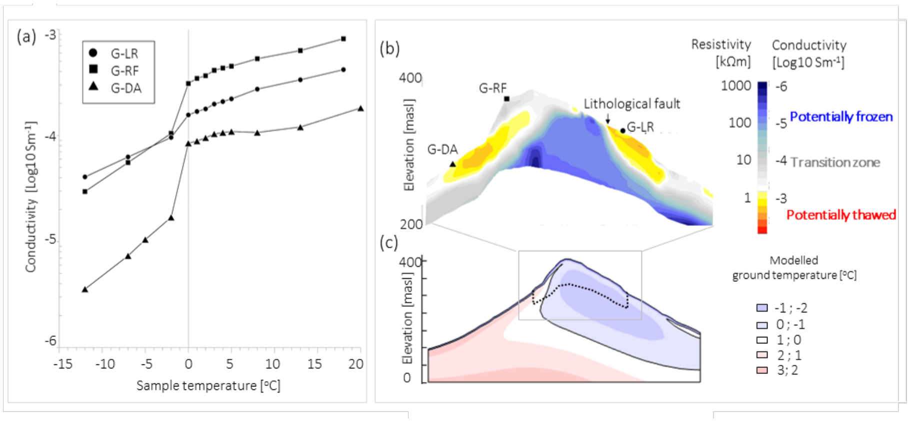

Figure 5. Comparison between ERT and 2D thermal model . ~~In panel~~ (a) ~~, the inverted conductivity model obtained by ERT on the field. On panel a, the results of the petrophysical~~ Petrophysical analysis, showing ~~the~~ in-phase electrical conductivity ~~range~~ data versus temperature for the ~~transition between frozen and unfrozen state. On panel (~~three samples collected along the geophysical profile; b) ~~the combination~~ profile of ~~the ERT inversion and petrophysical analysis, showing~~ electrical conductivity/resistivity tomography (in ~~blue colors expected frozen areas, while~~ Sm^{-1} and kΩm) measured on ~~yellow colors~~ the ~~expected unfrozen areas. On panel (~~field: c) ~~, the~~ resulting 2D numerical model of the ridge where the ERT line was conducted.

4.3 Modeling

4.3.1 GST Model

GST modeling is done at monthly time steps by aggregating weather forcing and on snow-free loggers data collected on bedrock (13 loggers available), averaged over monthly periods. The training results of the GST models are summarized by period in ~~Figure 4. Considering the dataset d, i.e. the dataset providing most climatic variables~~ Fig.6. For all datasets, we achieve similar performance in both training and validation sets, indicating good generalization power of the model~~even for high number of predictors~~. The prediction performance is best for dataset ~~d~~ b (R^2 = 0.98 and RMSE < 1.6 °C), while it is lower for the other datasets, reaching RMSE ~~2.46 –~~ 2.38 °C to 2.66 °C. On average, the presence of snow cover causes an offset on the MAGST of +1.58 °C ± 0.41 °C when other conditions do not change (R^2 = 0.81). We used this value of +1.58 °C, comparable to previous findings in Greenland (Rasmussen et al., 2018), as constant offset when modeling snow cover.

4.3.2 Heat transfer model

~~The~~ The model was calibrated by optimizing two parameters: matrix porosity and initial offset value. The optimal porosity was achieved for a value of 0.03, while the optimal initial offset was evaluated at +1.8 °C with respect to the average temperature on the period 1850-1860. Using these values, the model reaches a good agreement of the seasonal frost and heat penetration depths at SIS2021-01 for the period August 2021 – April 2022 (~~figure 5~~Fig.4a). The difference between model and data is consistently below 0.1 °C for depth below 10 m, while ~~in the active layer the model has disagreement~~ above the depth of zero

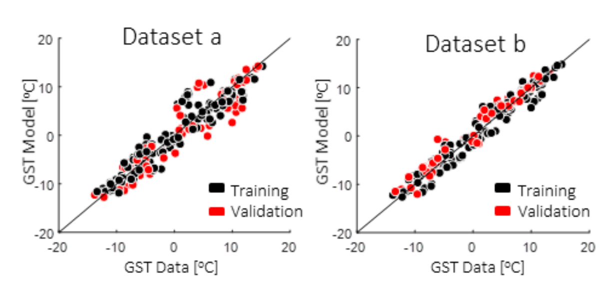

Dataset	Training R^2	Training RMSE	Val. R^2	Val. RMSE
a	0.95	2.46	0.95	2.46
b	0.98	1.45	0.98	1.46
c	0.95	2.39	0.95	2.38
d	0.94	2.65	0.94	2.66

Figure 6. GST models summary. On top, examples of model fit for the dataset ~~c~~ a (~~DMI~~ composite weather station data for 1850 – ~~2021~~2022) and ~~d~~ b (ERA5 reanalysis for 1979 – 2022). On bottom, table with training and validation performances for the four different GST models.

annual amplitude the model deviates up to 2 °C ~~with~~ from the measured data. When tested and compared to SIS2019-02 (z = ~~55m~~ 55 m ; PISR = 690 kWhm^{-2}, SnowP = 1), the model produces similar results (Fig.4b), indicating errors up to ~~few degrees in the active layer (10~~ 2 °C above the depth of zero annual amplitude (20 m depth), while ~~for depths below 20m~~ the errors are consistently ~~below~~ smaller than 0.15 °C below this depth.

~~Model compared to data at SIS2021. On left, temperature plot for the available measured period of both data and model results. On right, difference between model and measured temperatures. Cold colors indicate that the model is colder than the data, while warm colors indicate vice versa.~~

4.4 Permafrost mapping

The ~~GST model is run to produce boundary conditions for each cell in the DEM, which are used to run the heat transfer module. We obtain a database of monthly-averaged ground temperatures from 1850 to 2022 up to 100 m depth. This database can be used to produce several maps describing ground thermal conditions in the area, here we propose mean ground temperature (2012-2022)~~ permafrost map is represented by the MGT20, i.e. the average temperature at 20 ~~meters depth (~~m depth (below the dpeth of zero annual amplitude) during the period 2012-2022 (Fig.7a and b). Overall, the model indicates that 81 km^2 (57% of the study area) has negative MGT20~~– figure 6a, 6b) and summarize it~~. Spatial distribution of permafrost is summarized in a polar plot (~~figure 6c)~~Fig.7c), showing the relationship linking ground temperatures and the predictors aspect and elevation. At sea level, north facing ~~snow free~~ slopes can reach negative MGT20 when snow free. Negative MGT20 can be found on south slopes starting at 200 m.a.s.l.. ~~Snow cover plays an important role, as snow covered areas on steep south slopes (i.e. chutes), can have positive MGT20 up 450 masl, elevation at which permafrost is continuous.~~ The colder MGT20 ~~, which occur~~ occurs

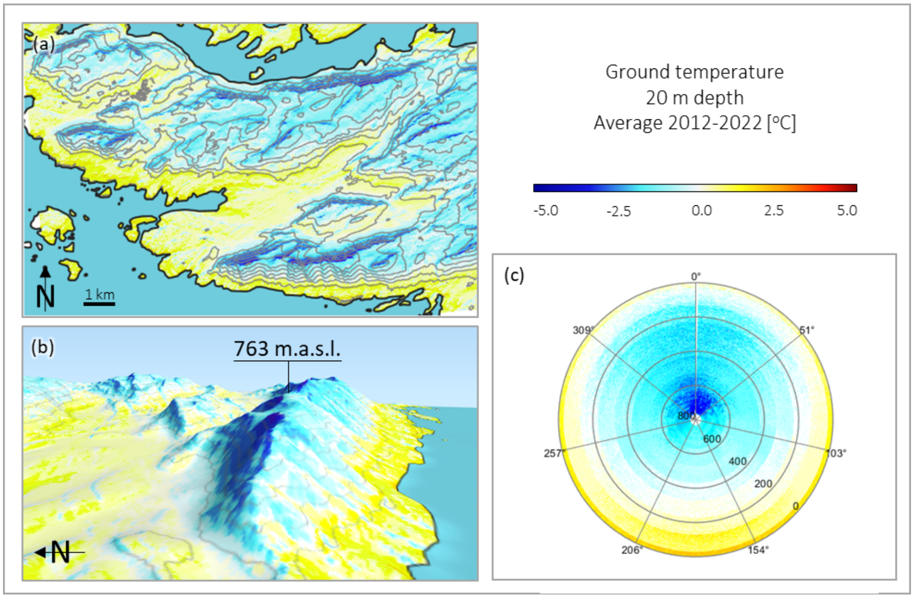

Figure 7. Summary of modelled ground temperature distribution in the study site. The parameters used to describe ground temperature here is the average ground temperature at 20 meters depth in the past ten years. On panel a, study site map colored by MGT20. On panel b, 3D view of the Nasaasaaq range from East. On panel c, polar plot of the distribution of MGT20 based on slope aspect (0° is ~~North~~north) and elevation (outer radius is sea level, increasing to 800 masl at the center.

on the north faces of the Nasaasaaq peak ~~-~~(763 m.a.s.l. ~~-~~), reaching -4.0 °C. Snow cover plays an important role, as snow covered areas can increase of 250 m the elevation of the MGT20 0 °C isotherm. This effect is prominent on mountain flanks characterized by sequences of ridges and chutes (Fig.7b), as the chutes are warmer than the ridges due to their predisposition to accumulate snow.

4.4.1 Comparison between 2D model ~~-~~and ERT profile

~~The~~ In Fig.5c is presented the 2D model simulation ~~on ERT1,~~ at the geophysical profile location. The model indicates, as of October 2020, the presence of ~~sporadic permafrost~~ negative temperatures below the depth of annual amplitude on the Nattoralinnguaq summit, suggesting the presence of permafrost. The south face is permafrost free, with ground temperatures above zero at 20-40 m depth. The north face on the other hand~~is permafrozen, reaching~~ , reaches temperatures below -1 °C. By comparing the model results with the ERT data (~~figure 7~~Fig.5b), we can observe a qualitative agreement between the two datasets, as they both indicate the presence of sporadic permafrost on the summit. Both datasets indicate a mostly unfrozen south face, and a colder north face. However, the ERT data indicate a large unfrozen section at the extremity of the north face~~,~~ ~~which is likely due the lithological fault observed on the field at this location~~.

4.4.2 Permafrost evolution in future scenarios: RCP 2.6 and RCP 8.5

Future scenarios simulations are conducted both at the landscape scale (Fig.8c) and at SIS2021-01 location (~~Figure 8a and 8b~~Fig.8a and 8b). The simulations conducted at SIS2021-01 show that, regardless the scenario used, permafrost conditions will disappear by the end of the ~~XXI~~ 21st century. For scenario RCP 2.6~~permafrost~~ , the ground seems in phase transition by 2100, being at 0.05 – 0.1 °C between 50 and 70 meters depth. For scenario RCP 8.5 ground temperatures are consistently above 0.3 °C~~, indicating total permafrost loss~~. In 2100, ground temperatures at ~~20-50m~~ 20-50 m depth are about 1 to 2.5 °C higher for the RCP 8.5 compared to RCP 2.6, indicating that, due to thermal inertia of the ground, surface heat is not yet fully propagated at depth by 2100 in this scenario.

At the landscape level, any future scenario causes a significant reduction in the extents of frozen grounds by 2100 (~~Figure 8c~~Fig.8c). For the ~~RCP2.6~~RCP 2.6, in 2090-2100 is simulated a slight increase in elevation of the MGT20 isotherm by about 150 m. This causes a widespread loss of permafrost grounds, from 81 km^2 (57% of the study area) to 53 km^2 (37%). For the scenario ~~RCP8.5~~ RCP 8.5 the impact on permafrost is more severe, as ~~permafrozen~~ permanently frozen ground disappears from most of the study area, except for the highest summits and covering ~~4km~~4 km^2 (3% of the study area) in the period 2090-2100. The MGT20 0 °C isotherm elevation increases above the 700 ~~masl~~ m.a.s.l. on south faces, while on north faces, we observe a retreat of the MGT20 0 °C isotherm ~~MGT20~~ up to 500 ~~masl.~~m.a.s.l..

A similar result is obtained when evaluating the expected ground temperature evolution in complex terrain ~~(figure 9).Nattoralinnguaq and Nasaasaaq present today sporadic and continuous permafrost respectively. Considering~~ by the 2D models (Fig.9).For Nattoralinnguaq, the optimistic scenario (RCP 2.6) ~~, the model suggests a significant~~ suggests an increase of ground temperatures ~~and a loss of permafrost grounds compared to present day's estimations, corresponding to aslight increase in elevation of the permafrost margins.~~of about 1 °C, causing permafrost retreat on the north face up to 200 m.a.s.l.. Scenario RCP 8.5 delineates a situation where ~~almost all~~ permafrost is relict, i.e. below the reach of seasonal frost ~~, except for~~ (Magnin et al., 2017a) , at approximately 100 m depth on the north face. The model produce similar results for Nasaasaaq, as for scenario RCP 2.6 we observe permafrost retreat to 300 m.a.s.l. on the north face ~~of the Nasaasaaq summit~~and to 500 m.a.s.l. on the south face. Scenario RCP 8.5 indicates that all permafrost on the mountain is relict, except for the summit's north face.

5 Discussion

5.0.1 ~~Model uncertainties and evaluation~~

~~Despite evaluating GST using an empirical approachhas been already used by several studies achieving good results (Magnin et al., 2017a; I , it involves strong assumptions~~

5.1 Model uncertainties and evaluation

Our modeling strategy is based on linking GST measurements to climate data downscaled with a topographical approach. Correlating GST with aspect and elevation only, as proxies of solar radiation and air temperature, disregards other processes

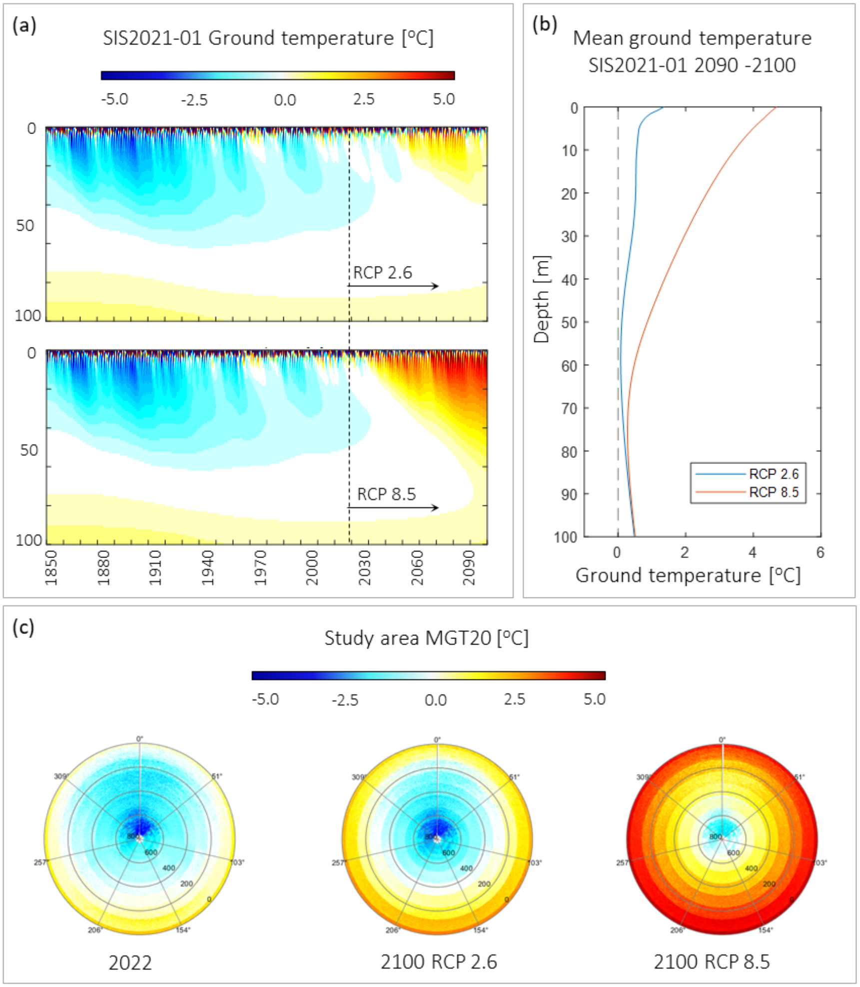

Figure 8. Summary of future scenarios from 1D models. ~~Panel a, ground~~ Ground temperature evolution at SIS2021-01 (a). ~~On panel b, comparison~~ Comparison of mean ground temperature profiles (2090-2100) between optimistic and pessimistic scenarios (b). ~~On panel c, landscape~~ Landscape distribution of MGT20 as polar plots (elevation as radius, angle as slope aspect – 0° points ~~North~~north) in 2022 and the two scenarios (c).

such as near surface air advection and longwave radiation. Although our method ~~is slightly more complex as it~~ also involves other weather parameters for the period 1979-2022, the basic assumption of linear relation between GST and topographical settings still holds.

To better contextualize our ~~result~~results, we can compare our model to ~~?~~ Schmidt et al. (2021) which represents the state of the art of numerical modeling of the physical processes affecting rockwall temperature in the arctic. Their approach is based on the SEB module of ~~Cryogrid~~ CryoGrid 3 modified to account for vertical terrain, including vertical moisture transport

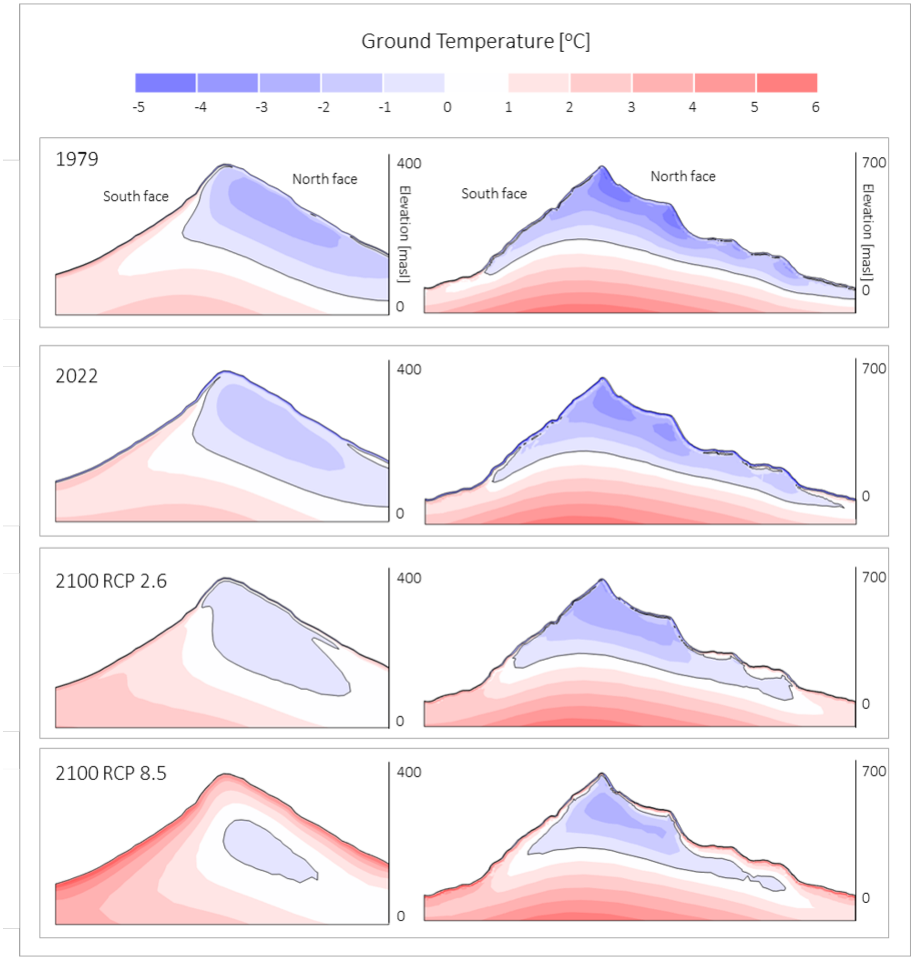

Figure 9. Modelled evolution of ground temperatures on Nattoralinnguaq (left column) and Nasaasaaq (right column). The images are ~~issued form~~ computed using the 2D ~~models~~model of ground temperature evolution.

affected by latent heat flux and ~~skiview~~ skyview factor adapted to steep terrain. By comparing model runs and field data, ~~?~~ Schmidt et al. (2021) obtained R^2 = 0.97 and RMSE = 1.2 °C on monthly GST data, which is comparable to our model performance on the validation dataset c (R^2 = 0.99 and RMSE = 1.6 °C). Although this comparison is encouraging, we suggest that the time period covered by our data is still too short (only one year) to fully understand the predictive performance of our ~~model. Maintaining the operational the GSTmonitoring network and updating the model as time passes will be crucial to define with more confidence this source of uncertainty~~modeling approach for GST.

~~Another source of uncertainty is due to snow accumulation. Snow is known to cause severe disturbance to GST, which can significantly affect active layer thickness even when accumulating in isolated patches (Magnin et al., 2017b). Although our estimated offset is comparable to previous findings in Greenland (Rasmussen et al., 2018), models are extremely sensitive to snow characteristics (Etzelmüller et al., 2022a), causing estimation of permafrost extents to greatly vary depending on~~

~~the modeling assumptions (Czekirda et al., 2019). Additionally, the offset method disregards snow physics as melting of the snowpack, layers metamorphism, and coupled interactions at the ground-snow interface. This method is incapable to explain how snow can sometimes cool the ground depending on the timing of its onset and its persistence during early heatwaves (Lerjen et al., 2003).~~

~~Typically, snow free areas are outlined by applying a filter snow/no snow area using a slope threshold (Magnin et al., 2019). Our snow probability map proposes a description of snow accumulation in steep chutes and snow absence on flat wind-exposed outcrops. Overall, this approach, provides a good idea on how and where ground temperatures are influenced by snow cover at the large scale. Although we do not have enough data to validate this approach, it is encouraging that the SnowP map provides an acceptable boundary condition to model deep ground temperature in the snow-affected borehole SIS2019-02 and snow-free~~ A more reliable assessment of the model performance is given by comparing the results of the heat transfer module to the borehole ~~SIS2021-01.~~

~~To provide a more detailed quantification of such processes, various numerical algorithms as CryoGrid, Snowpack and Crocus, are used to describe large scale – hectometric resolution permafrost distribution (Gisnås et al., 2014). At this resolution and scale, it is possible to obtain relevant information on snow characteristics using remote sensing data. Nevertheless, when dealing with the metric resolution required to successfully model steep bedrock permafrost, it becomes extremely challenging to achieve a good knowledge of spatial characteristics of the snow, given the spatial variability of snow redistribution by wind. This issue has discouraged most authors to use a numerical method to approach the problem. Nevertheless, some studies ventured into a detailed modeling of such process at a smaller scale – decimeter resolution – for selected slopes.In particular, Haberkorn et al. (2016) proposed the combination of repeated Terrestrial Laser Scanning and Alpine3D to finely model (0.2 m resolution)snow deposition on steep terrain and its influence on the rockwall surface temperature. Although such approach is not directly applicable at our scale, this framework seems to be the right approach to provide detailed knowledge of a selected slope of interest. In this sense, the offset method used in this study is relevant to provide a general frame of the influence of snow on ground temperatures at the large scale, while a more detailed approachis recommended when dealing with site-specific situations.~~

5.2 ~~Heat transfer modelling~~

~~Our heat transfer module is representative for isotropic bedrock as it does not consider anisotropic thermal conductivity caused by rock porosity. Therefore, sediments, vegetation patches, debris and individual large fractures are not correctly modelled and will need a dedicated mapping and modelling effort to compute a complete permafrost map of the area. Concerning bedrock, factures can either warm the bedrock through water advection, while air circulation can cool the bedrock (Hasler et al., 2011). Ice cemented fractures are major drivers in permafrost aggradation and degradation, and their behavior is not representable by a simple conductive approach (Hasler et al., 2012). Fractures delay permafrost degradation when bedrock is warming, but assoon as ice begins to thaw, they create thawing preferential corridors (Magnin et al., 2020). Furthermore, ice cemented fractures are major drivers in bedrock permafrost stability (Hasler et al., 2012) as their thermal behavior create strong anisotropies in~~

~~the hydraulic head and fluid pressure (Magnin et al., 2020). Therefore understanding their behavior is not only relevant for correctly model ground thermodynamics, but also slope stability.~~

~~Another major limitation is due to the use of a 1D model for the mapping module, which disregards lateral influences. Although the mountain terrain near Sisimiut is mostly gentle, we expect our map to be imprecise in the proximity of sharp slope breaks and ridges. 2D models~~ and geophysical data. Although our model seems to provide good results (mean error of 0.14 °C from 0 to 100 m depth, Fig.4), we shall compare our results to Magnin et al. (2017a), who use a similar modeling approach, to better understand this performance. It must be taken into account that a direct comparison is difficult as, in our case boreholes are on flat terrain, which are influenced by lateral variations in snow accumulation and surface characteristics. Magnin et al. (2017a) on the other hand ~~provide a much stronger approximation in complex terrain, as they provide similar results for 3D transient simulations (Noetzli et al., 2007). In this sense, representative 2D transects seem adequate to describe and predict permafrost evolution patterns in complex terrain, unloading computational efforts. Overall, our approach is adapted to provide a large-scale and computationally efficient evaluation of permafrost characteristics using a numerical approach. However, when more detail is required in a specific site, more sophisticated approaches exist. In particular, the new approach described by (Magnin et al., 2020) seems to overcome most of the aforementioned issues. Their approach describes thermal process in fractured bedrock using a quantitative numerical approach in FeFlow. Deep fractures are directly represented in the model mesh and their geometry can be evaluated by lithological interpretation of dip angle of main surface discontinuities (Mamot et al., 2020) or by Seismic Refraction Tomography (Phillips et al., 2016). These approaches are advised for selected study sites with high relevance, justifying the effort of collecting the data required to run the – CPU intensive – numerical model.~~

5.2 ~~Global performance~~

~~To have an idea of the overall performance of our model, we can compare our results to Magnin et al. (2017a) which use a comparable approach. Magnin et al. (2017a),~~ have data from boreholes on drilled vertical bedrock, arguably less influenced by lateral variability in ground characteristics and snow cover. Given this, Magnin et al. (2017a) reaches an average difference between modelled and measured temperatures ~~at 10m depth~~ of 0.01 °C at 10 m depth, indicating a ~~significantly~~ better performance than our model. Since most of the disagreement between ~~our model and measured data occurs above 10m depth~~borehole data and our model occur in the upper 10 m, we believe that ~~, this~~ this performance difference is likely imputable to our climatic database. While Magnin et al. (2017a) ~~disposed of~~ had near-in situ long term weather ~~stations~~station data, our data ~~which seems~~ come mostly from global reanalysis, and seem to be not precise enough to explain ~~short-time~~ short-term variability in ground temperatures. ~~Also, our boreholes are on flat terrain, which are influenced by lateral variations in snow accumulation and surface characteristics, while Magnin et al. (2017a) dispose of boreholes on vertical bedrock. These different surfaces are expected to create lateral influences on the borehole 1D column, causing deviations from the ideal isotropic conditions simulated by our model . Finally, our model is based only on one year of data coverage, which is likely a too short time period for achieving a full understanding of the processes involved and a proper calibration of the GST models~~Overall, we suggest that our model is not suitable for describing short term variability of ground temperatures above the depth of zero annual amplitude.

~~Given this, our results indicate that the model describes within 0.1 C deep ground temperatures (below 10m meters) for SIS2021-01 and similar values are achieved on the validation borehole SIS2019-02. Since SIS2019-02 was not used for numerical model calibration, we have good confidence in estimating an expected uncertainty of 0.1-0.2~~ On the other hand, our model is more reliable when describing ground temperatures below the depth of zero annual amplitude. Here, the model has a maximum error of 0.15 °C when ~~estimating deep temperatures. This performance is satisfactory as it suggest that the model fulfills the study's aim to describe general bedrock permafrost conditions in the area with acceptable confidence. This conclusion is also supported by the comparison between our 2D model and the ERT inversion jointed with petrophysical analysis. Considering that the unfrozen area~~ compared to SIS2019-02, which is used only as validation dataset. SIS2019-02 has also different snow conditions than SIS2021-01, suggesting that our SnowP map and offset provide an acceptable boundary condition to model long term effect of recurrent snow cover induced by topographical patterns. The general agreement between model and geophysical data also indicates that the model is suitable for describing permafrost extents in a wide range of elevations, slopes and aspects. Most of the disagreement between model and data is due to the electrical conductivity anomaly on the north face ~~indicated by the ERT is likely due to a lithological fault observed on the field, indicating that the petrophysical analysis and isotropic assumption is not valid in this area, there is an overall qualitative agreement between ERT and numerical simulation.~~ of the geophysical profile. This anomaly occurs near a large lithological fault, visible in the field. Overall, the observations indicate that ground characteristics at this location are not isotropic and a direct comparison between model and geophysics is not meaningful. All this considered, the results indicate that the modeling approach is suitable for evaluating of ground temperatures below the depth of zero annual amplitude in complex terrain. This is achieved with using forcing data available at the Greenland scale, making an significant step towards a comprehensive assessment of mountain permafrost in the region.

5.2 ~~Present-day bedrock permafrost characteristics compared to other regions~~

~~Keeping in mind the limitations we discussed above, we~~

5.2 Local permafrost distribution compared to other regions

We can use our results to ~~discuss the general characteristics~~ compare the distribution of bedrock permafrost in the Sisimiut area ~~and their future evolution.~~to other mountain ranges, as presented in Fig.10. Ground surface temperatures in rockwalls seems comparable to conditions described in Northern Norway (69 – 71° N), where permafrost can be found at sea level ~~as sporadic~~ on north facing slopes (Magnin et al., 2019). In Sisimiut, the solar radiation creates an average offset of 2.4 °C from ~~North to South~~ north to south facing slopes, causing a rise of about 400 m of elevation in the permafrost 0 °C isotherm between this two aspects. This offset is known to be dependent on latitude, varying from 8 °C ~~m~~ in the European Alps (45-46° N, Magnin et al. (2015a)) to 1.5 °C in Northern Norway (69-71° N, Magnin et al. (2019)~~, Figure 10~~). In coastal climates, previous studies suggested that steep bedrock permafrost could be influenced by other factors than pure solar radiation, as cloudiness and icing, creating an abnormally low offset in New Zealand (Allen et al., 2009). In this context, the ~~North-South offset we measured~~ north-south offset we measure in the Sisimiut area is consistent with the latitudinal trend obtainable by

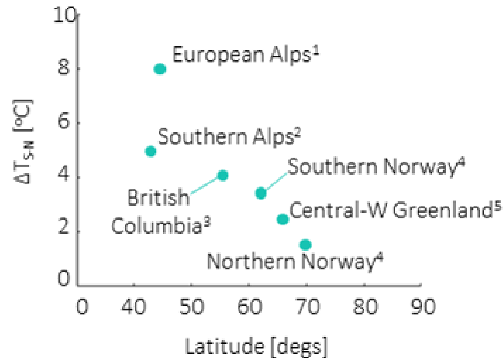

Figure 10. Temperature offset between north and south facing rockwalls at different latitudes, retrieved from Magnin et al. (2015a)[1], Allen et al. (2009)[2], Hasler et al. (2015)[3], Magnin et al. (2019)[4] and the present study[5].

previous studies, suggesting that, despite the fact that the Sisimiut mountain area is coastal, pure solar radiation is dominant on landscape-scale permafrost characteristics, after elevation-dependent air temperature variations.

5.3 Future evolution of bedrock permafrost in the area and implications

Our model suggests that as of 2020 the deep ground temperatures are in disequilibrium with the current climate. This is highlighted by the fact that, even in scenario ~~RCP2.6~~RCP 2.6, which causes a relatively mild increase in air temperatures and MGT20, the ~~permafrozen~~ permanently frozen bedrock area will decrease by about 35% by 2090-2100. This corresponds to the disappearance of permafrost in most low elevation south facing slopes and plateaus, as well as an increase of the active layer thickness for most of north facing slopes at low elevation. This situation becomes more ~~and more~~ critical with scenario ~~RCP8.5~~RCP 8.5, where only 5% of permafrost ground existent in 2022 will ~~survive to the end of the XXI~~ outlast the 21st century. As highlighted by the 2D simulations, this does not involve a dramatic reduction of the deep frozen bodies, as they will persist in form of relict permafrost well after the end of the ~~XXI even in the pessimistic scenario~~21st century. These results are comparable to the French Alps where mountain permafrost is expected to retreat only on the highest summits of the Mont Blanc massif, while relict permafrozen bedrock can persist at lower elevations (Magnin et al., 2017a).

~~Our~~ These findings imply that in the near future permafrost degradation will affect most of the rockwalls in the Sisimiut area, creating the preliminary conditions for a possible increase in rockfall activity of both small and large magnitude (Krautblatter et al., 2013). ~~Although the correlation between permafrost degradation and rockfall activity is accepted within the scientific community (Ravanel and Deline, 2011; Patton et al., 2019), the process chain linking the two phenomena is very complex. In general, permafrost degradation causes a progressive deepening of the frozen body, increasing water circulation in cracks and weakening of the mechanical properties of the ice-bedrock matrix (Davies et al., 2001; Krautblatter et al., 2013). This does~~

~~not mean that we automatically expect an increase of rockfall activity in the area, as lithological predisposition to failure, as factures dip versus slope, is the major control on stability. In addition, water infiltration patterns play a role in stability, as rainwater may infiltrate the bedrock while snow meltwater cannot percolate in case of ice basal layer (Phillips et al., 2016). Based on our results, we suggest that, for those areas already known for existing rockfall activity and highlighted by our model as expecting severe permafrost degradation, future efforts should be made to better assess rock slope stability.~~

6 Conclusions

This study presents a first quantification of bedrock permafrost on mountain terrain in Sisimiut, West Greenland, using a heat transfer module forced by simplified weather data. The modeling approach produces results that are consistent with available data from deep boreholes and geophysical investigations. Based on our results, permafrozen bedrock can be found at sea level on north facing/snow free slopes, while on south facing slopes the lower margins are at about 400 m.a.s.l.. This indicates that, considering the local topography, most of the mountain terrain hosts temperate permafrost. Forcing our model with future climatic projections shows different degrees of permafrost degradation ~~based~~ depending on the scenario ~~used~~considered. For scenario ~~RCP8.5~~RCP 8.5, i.e. with no mitigation on carbon emissions, our model predicts a reduction of 95% of the active permafrost area at the end of the century, meaning that ~~permafrozen~~ permanently frozen ground will persist only as relict condition ~~at depthgreater than~~ below 10-20 m depth, i.e. below the reach of the seasonal frost. This condition ~~suggest~~ suggests a future strong disequilibrium between ground ~~thermal conditions~~ temperatures and climatic forcing~~. Future~~ , creating the basis for more frequent rockfall activity. Although the correlation between permafrost degradation and rockfall activity is accepted within the scientific community (Ravanel and Deline, 2011; Patton et al., 2019), the process chain linking the two phenomena is very complex. Therefore, future efforts in the area should focus on investigating slope stability characteristics, and their relation to ~~permafrozen conditions~~permafrost distribution and degradation. Once (and if) problematic slopes are identified, site specific models integrating high resolution snow distribution ~~and crack mapping~~ (Haberkorn et al., 2016) and crack networks (Magnin et al., 2020) will provide a more detailed understanding of slope thermodynamics, overcoming the main uncertainties of our model. Further efforts should also apply at larger scale, in order to characterize mountain permafrost in the whole region. In this sense, our modeling approach based on ~~few weather parameters~~ weather parameters readily available for the whole region, downscalable with a simple topographical approach, provides a good ~~trade-off between results quality and uncertainty~~first assessment for mountain permafrost zonation.

Data availability. Ground temperature data are available at: Marcer, Marco (2022): Dataset - Bedrock Permafrost in Greenland. Technical University of Denmark. Dataset. https://doi.org/10.11583/DTU.21215591

Author contributions. MM designed the study, conducted fieldwork and modeling. PAD conducted geophysical fieldwork and data processing. ST participated in geophysical fieldwork. SRN organised deep boreholes drillings. AR advised on geophysical data processing. TIN supervised the study, field logistics and data interpretation. All authors contributed to the manuscript.

Competing interests. No competing interests are present

Acknowledgements. This study is part of project TEMPRA and Siku Aajiutsoq, funded by the Greenland Research Council. The study is also part of the Nunataryuk project, which is funded under the European Union's Horizon 2020 Research and Innovation Programme under Grant Agreement 773421. The deep boreholes were established as part of the Greenland Integrated Observing System (GIOS) funded by the Danish National Fund for Research Infrastructure (NUFI) under the Ministry for higher Education and Science. This work was realised in cooperation with EDYTEM and ~~Styx 4D~~Styx4D. We acknowledge Jessy Lossel for his work on the rock samples.

References

Allen, S. K., Gruber, S., and Owens, I. F.: Exploring Steep Bedrock Permafrost and its Relationship with Recent Slope Failures in the Southern Alps of New Zealand, 356, 345–356, https://doi.org/10.1002/ppp, 2009.

Bentsen, M., Bethke, I., Debernard, J. B., Iversen, T., Kirkevåg, A., Seland, Ø., Drange, H., Roelandt, C., Seierstad, I. A., Hoose, C., and Kristjánsson, J. E.: The Norwegian Earth System Model, NorESM1-M – Part 1: Description and basic evaluation of the physical climate, Geoscientific Model Development, 6, 687–720, https://doi.org/10.5194/gmd-6-687-2013, 2013.

Biskaborn, B. K., Smith, S. L., Noetzli, J., Matthes, H., Vieira, G., Streletskiy, D. A., Schoeneich, P., Romanovsky, V. E., Lewkowicz, A. G., Abramov, A., Allard, M., Boike, J., Cable, W. L., Christiansen, H. H., Delaloye, R., Diekmann, B., Drozdov, D., Etzelmüller, B., Grosse, G., Guglielmin, M., Ingeman-Nielsen, T., Isaksen, K., Ishikawa, M., Johansson, M., Johannsson, H., Joo, A., Kaverin, D., Kholodov, A., Konstantinov, P., Kröger, T., Lambiel, C., Lanckman, J. P., Luo, D., Malkova, G., Meiklejohn, I., Moskalenko, N., Oliva, M., Phillips, M., Ramos, M., Sannel, A. B. K., Sergeev, D., Seybold, C., Skryabin, P., Vasiliev, A., Wu, Q., Yoshikawa, K., Zheleznyak, M., and Lantuit, H.: Permafrost is warming at a global scale, Nature Communications, 10, 1–11, https://doi.org/10.1038/s41467-018-08240-4, 2019.

Boeckli, L., Brenning, A., Gruber, S., and Noetzli, J.: Permafrost distribution in the European Alps: calculation and evaluation of an index map and summary statistics, The Cryosphere, 6, 807–820, https://doi.org/10.5194/tc-6-807-2012, 2012.

Cappelen, J. and Jensen, D.: Climatological Standard Normals 1991-2020 - Greenland, Tech. rep., DMI - Danish Meteorological Institute, https://www.dmi.dk/publikationer/, 2021.

Cappelen, J., Vinther, B. M., Kern-Hansen, C., Laursen, E. V., and Jørgensen, P. V.: Greenland-DMI Historical Climate Data Collection 1784-2020, Tech. Rep. May, www.dmi.dkwww.dmi.dkurlhttps://www.dmi.dk/publikationer/www.dmi.dk, 2021.

Colgan, W., Rajaram, H., Abdalati, W., McCutchan, C., Mottram, R., Moussavi, M. S., and Grisby, S.: Glacier crevasses: Observations, models, and mass balance implications, Reviews of Geophysics, 54, 119–161, https://doi.org/doi:10.1002/2015RG000504, 2016.

COMSOL Inc.: COMSOL Multiphysics, Heat Transfer Module User's Guide, version 5.4, https://doc.comsol.com/5.4/doc/com.comsol.help.heat/HeatTransferModuleUsersGuide.pdf, 2015.

Conrad, O., Bechtel, B., Bock, M., Dietrich, H., Fischer, E., Gerlitz, L., Wehberg, J., Wichmann, V., and Böhner, J.: System for Automated Geoscientific Analyses (SAGA) v. 2.1.4, Geoscientific Model Development, 8, 1991–2007, https://doi.org/10.5194/gmd-8-1991-2015, 2015.

Czekirda, J., Westermann, S., and Etzelmüller, B.: Transient Modelling of Permafrost Distribution in Iceland, 7, 1–23, https://doi.org/10.3389/feart.2019.00130, 2019.

Daanen, R. P., Ingeman-Nielsen, T., Marchenko, S. S., Romanovsky, V. E., Foged, N., Stendel, M., Christensen, J. H., and Hornbech Svendsen, K.: Permafrost degradation risk zone assessment using simulation models, Cryosphere, 5, 1043–1056, https://doi.org/10.5194/tc-5-1043-2011, 2011.

Dahlin, T. and Zhou, B.: A numerical comparison of 2D resistivity imaging with 10 electrode arrays, Geophysical Prospecting, 52, 379–398, https://doi.org/10.1111/j.1365-2478.2004.00423.x, 2004.

Davies, M., Hamza, O., and Harris, C.: The effect of rise in mean annual temperature on the stability of rock slopes containing ice-filled discontinuities, Permafrost Periglacial Processes, 12, 137–144, 2001.

Duvillard, P. A., Ravanel, L., Marcer, M., and Schoeneich, P.: Recent evolution of damage to infrastructure on permafrost in the French Alps, Regional Environmental Change, 19, 1281–1293, https://doi.org/10.1007/s10113-019-01465-z, 2019.

Duvillard, P.-A., Magnin, F., Revil, A., Legay, A., Ravanel, L., Abdulsamad, F., and Coperey, A.: Temperature distribution in a permafrost-affected rock ridge from conductivity and induced polarization tomography, Geophysical Journal International, pp. 1207–1221, https://doi.org/10.1093/gji/ggaa597, 2020.

Etzelmüller, B.: Recent advances in mountain permafrost research, Permafrost and Periglacial Processes, 24, 99–107, https://doi.org/10.1002/ppp.1772, 2013.

Etzelmüller, B., Czekirda, J., Magnin, F., Duvillard, P.-a., Malet, E., Ravanel, L., Aspaas, A., Kristensen, L., Skrede, I., Leinauer, J., Hauck, C., Hilbich, C., Hermanns, R., Krautblatter, M., Westermann, S., Bourget-du lac, L., and Water, N.: Permafrost in monitored unstable rock slopes in Norway – New insights from rock wall temperature monitoring , geophysical surveying and numerical modelling, Earth Surface Dynamics Discussions, 10, 2022a.

Etzelmüller, B., Czekirda, J., Magnin, F., Duvillard, P. A., Ravanel, L., Malet, E., Aspaas, A., Kristensen, L., Skrede, I., Majala, G. D., Jacobs, B., Leinauer, J., Hauck, C., Hilbich, C., Böhme, M., Hermanns, R., Eriksen, H. O., Lauknes, T. R., Krautblatter, M., and Westermann, S.: Permafrost in monitored unstable rock slopes in Norway-New insights from temperature and surface velocity measurements, geophysical surveying, and ground temperature modelling, Earth Surface Dynamics, 10, 97–129, https://doi.org/10.5194/esurf-10-97-2022, 2022b.

Fettweis, X., Mabille, G., Erpicum, M., Nicolay, S., and van den Broeke, M.: The 1958-2009 Greenland ice sheet surface melt and the mid-tropospheric atmospheric circulation, Climate Dynamics, 36, 139–159, https://doi.org/10.1007/s00382-010-0772-8, 2011.

Frauenfelder, R., Isaksen, K., Lato, M. J., and Noetzli, J.: Ground thermal and geomechanical conditions in a permafrost-affected high-latitude rock avalanche site (Polvartinden, northern Norway), Cryosphere, 12, 1531–1550, https://doi.org/10.5194/tc-12-1531-2018, 2018.

Gallach, X., Carcaillet, J., Ravanel, L., Deline, P., Ogier, C., Rossi, M., Malet, E., and Garcia-Sellés, D.: Climatic and structural controls on Late-glacial and Holocene rockfall occurrence in high-elevated rock walls of the Mont Blanc massif (Western Alps), Earth Surface Processes and Landforms, 45, 3071–3091, https://doi.org/10.1002/esp.4952, 2020.

Gisnås, K., Westermann, S., Schuler, T. V., Litherland, T., Isaksen, K., Boike, J., and Etzelmüller, B.: A statistical approach to represent small-scale variability of permafrost temperatures due to snow cover, Cryosphere, 8, 2063–2074, https://doi.org/10.5194/tc-8-2063-2014, 2014.

Gisnås, K., Etzelmüller, B., Lussana, C., Hjort, J., Sannel, A. B. K., Isaksen, K., Westermann, S., Kuhry, P., Christiansen, H. H., Frampton, A., and Åkerman, J.: Permafrost Map for Norway , Sweden and Finland, Permafrost and Periglacial Processes, 28, 359–378, https://doi.org/10.1002/ppp.1922, 2017.

Gruber, S.: Derivation and analysis of a high-resolution estimate of global permafrost zonation, Cryosphere, 6, 221–233, https://doi.org/10.5194/tc-6-221-2012, 2012.

Gruber, S., Hoelzle, M., and Haeberli, W.: Rock-wall temperatures in the Alps: Modelling their topographic distribution and regional differences, Permafrost and Periglacial Processes, 15, 299–307, https://doi.org/10.1002/ppp.501, 2004.

Gubler, S., Fiddes, J., Keller, M., and Gruber, S.: Scale-dependent measurement and analysis of ground surface temperature variability in alpine terrain, The Cryosphere, 5, 431–443, https://doi.org/10.5194/tc-5-431-2011, 2011.

Guerin, A., Ravanel, L., Matasci, B., Jaboyedoff, M., and Deline, P.: The three-stage rock failure dynamics of the Drus (Mont Blanc massif, France) since the June 2005 large event, Scientific Reports, 10, 1–21, https://doi.org/10.1038/s41598-020-74162-1, 2020.

Haberkorn, A., Wever, N., Hoelzle, M., Phillips, M., Kenner, R., Bavay, M., and Lehning, M.: Distributed snow and rock temperature modelling in steep rock walls using Alpine3D, The Cryosphere Discussions, pp. 1–30, https://doi.org/10.5194/tc-2016-73, 2016.

Haeberli, W., Arenson, L., Delaloye, R., Gruber, S., Isaksen, K., Kneisel, C., Krautblatter, M., Noetzli, J., Phillips, M., and Division, C.: Permafrost on mountain slopes – development and challenges of a young research field, Environmental Research, 56, 1043–1058, https://doi.org/10.3189/002214311796406121, 2010.

Hasler, A., Gruber, S., and Haeberli, W.: Temperature variability and offset in steep alpine rock and ice faces, Cryosphere, 5, 977–988, https://doi.org/10.5194/tc-5-977-2011, 2011.

Hasler, A., Gruber, S., and Beutel, J.: Kinematics of steep bedrock permafrost, Journal of Geophysical Research: Earth Surface, 117, 1–17, https://doi.org/10.1029/2011JF001981, 2012.

Hasler, A., Geertsema, M., Foord, V., Gruber, S., and Noetzli, J.: The influence of surface characteristics , topography and continentality on mountain permafrost in British Columbia, The Cryosphere, 9, 1025–1038, https://doi.org/10.5194/tc-9-1025-2015, 2015.

Hersbach, H., Bell, B., Berrisford, P., Hirahara, S., Horányi, A., Muñoz-Sabater, J., Nicolas, J., Peubey, C., Radu, R., Schepers, D., Simmons, A., Soci, C., Abdalla, S., Abellan, X., Balsamo, G., Bechtold, P., Biavati, G., Bidlot, J., Bonavita, M., De Chiara, G., Dahlgren, P., Dee, D., Diamantakis, M., Dragani, R., Flemming, J., Forbes, R., Fuentes, M., Geer, A., Haimberger, L., Healy, S., Hogan, R. J., Hólm, E., Janisková, M., Keeley, S., Laloyaux, P., Lopez, P., Lupu, C., Radnoti, G., de Rosnay, P., Rozum, I., Vamborg, F., Villaume, S., and Thépaut, J. N.: The ERA5 global reanalysis, Quarterly Journal of the Royal Meteorological Society, 146, 1999–2049, https://doi.org/10.1002/qj.3803, 2020.

Hipp, T., Etzelmüller, B., and Westermann, S.: Permafrost in Alpine Rock Faces from Jotunheimen and Hurrungane, Southern Norway, Permafrost and Periglacial Processes, 25, 1–13, https://doi.org/10.1002/ppp.1799, 2014.

Hofer, S., Lang, C., Amory, C., Kittel, C., Delhasse, A., Tedstone, A., and Fettweis, X.: Greater Greenland Ice Sheet contribution to global sea level rise in CMIP6, Nature Communications, 11, 1–11, https://doi.org/10.1038/s41467-020-20011-8, 2020.

Isaksen, K., Lutz, J., Sørensen, A. M., Godøy, Ø., Ferrighi, L., Eastwood, S., and Aaboe, S.: Advances in operational permafrost monitoring on Svalbard and in Norway, Environmental Research Letters, 17, https://doi.org/10.1088/1748-9326/ac8e1c, 2022.

Kneisel, C.: Assessment of subsurface lithology in mountain environments using 2D resistivity imaging, Geomorphology, 80, 32–44, https://doi.org/10.1016/j.geomorph.2005.09.012, 2006.

Krautblatter, M. and Hauck, C.: Electrical resistivity tomography monitoring of permafrost in solid rock walls, Journal of Geophysical Research: Earth Surface, 112, 1–14, https://doi.org/10.1029/2006JF000546, 2007.

Krautblatter, M., Funk, D., and Günzel, F. K.: Why permafrost rocks become unstable: A rock-ice-mechanical model in time and space, Earth Surface Processes and Landforms, 38, 876–887, https://doi.org/10.1002/esp.3374, 2013.

Legay, A., Magnin, F., and Ravanel, L.: Rock temperature prior to failure: Analysis of 209 rockfall events in the Mont Blanc massif (Western European Alps), Permafrost and Periglacial Processes, 32, 520–536, https://doi.org/10.1002/ppp.2110, 2021.

Lerjen, M., Kääb, A., Hoelzle, M., and Haeberli, W.: Local distribution pattern of discontinuous mountain permafrost. A process study at Flüela Pass, Swiss Alps, Proceedings of the 8th International Conference on Permafrost, 21-25 July 2003, Zurich, Switzerland, pp. 21–25, http://folk.uio.no/kaeaeb/publications/icop03_lerjen.pdf, 2003.

Ljungdahl, B.: Geologisk oversigt: Grønland, 1967.

Loke, M. H. and Barker, R. D.: Rapid least-squares inversion of apparent resistivity pseudosections by a quasi-Newton method, Geophysical Prospecting, 44, 131–152, https://doi.org/10.1111/j.1365-2478.1996.tb00142.x, 1996.

Magnin, F., Deline, P., Ravanel, L., Noetzli, J., and Pogliotti, P.: Thermal characteristics of permafrost in the steep alpine rock walls of the Aiguille du Midi (Mont Blanc Massif, 3842 m a.s.l), Cryosphere, 9, 109–121, https://doi.org/10.5194/tc-9-109-2015, 2015a.

Magnin, F., Krautblatter, M., Deline, P., Ravanel, L., Malet, E., and Bevington, A.: Determination of warm, sensitive permafrost areas in near-vertical rockwalls and evaluation of distributed models by electrical resistivity tomograph, Journal of Geophysical Research: Earth Surface, 120, 2452–2475, https://doi.org/10.1002/2014JF003351.Received, 2015b.

Magnin, F., Josnin, J. Y., Ravanel, L., Pergaud, J., Pohl, B., and Deline, P.: Modelling rock wall permafrost degradation in the Mont Blanc massif from the LIA to the end of the 21st century, Cryosphere, 11, 1813–1834, https://doi.org/10.5194/tc-11-1813-2017, 2017a.

Magnin, F., Westermann, S., Pogliotti, P., Ravanel, L., Deline, P., and Malet, E.: Snow control on active layer thickness in steep alpine rock walls (Aiguille du Midi, 3842 m a.s.l., Mont Blanc massif), Catena, 149, 648–662, https://doi.org/10.1016/j.catena.2016.06.006, 2017b.

Magnin, F., Etzelmüller, B., Westermann, S., Isaksen, K., Hilger, P., and Hermanns, R. L.: Permafrost distribution in steep slopes in Norway: measurements, statistical modelling and geomorphological implication, Earth Surface Dynamics Discussions, pp. 1–35, https://doi.org/10.5194/esurf-2018-90, 2019.

Magnin, F., Josnin, J., Magnin, F., Water, J. J., Permafrost, R., and Coupling, A.: Water Flows in Rockwall Permafrost : a Numerical Approach Coupling Hydrological and Thermal Processes To cite this version : HAL Id : hal-03024087 Water Flows in Rockwall Permafrost : a Numerical Approach Coupling Hydrological, 2020.

Mamot, P., Weber, S., Eppinger, S., and Krautblatter, M.: Stability assessment of degrading permafrost rock slopes based on a coupled thermo-mechanical model, Earth Surface Dynamics Discussions, pp. 1–45, https://doi.org/10.5194/esurf-2020-70, 2020.

Marcer, M., Stentoft, P. A., Bjerre, E., Cimoli, E., Bjørk, A., Stenseng, L., and Machguth, H.: Three Decades of Volume Change of a Small Greenlandic Glacier Using Ground Penetrating Radar, Structure from Motion, and Aerial Photogrammetry, Arctic, Antarctic, and Alpine Research, 49, 411–425, https://doi.org/10.1657/AAAR0016-049, 2017.

Marcer, M., Cicoira, A., Cusicanqui, D., Bodin, X., Echelard, T., Obregon, R., and Schoeneich, P.: Rock glaciers throughout the French Alps accelerated and destabilised since 1990 as air temperatures increased, Communications Earth Environment, pp. 1–12, https://doi.org/10.1038/s43247-021-00150-6, 2021.

Myhra, K. S., Westermann, S., and Etzelmüller, B.: Modelled Distribution and Temporal Evolution of Permafrost in Steep Rock Walls Along a Latitudinal Transect in Norway by CryoGrid 2D, 182, 172–182, https://doi.org/10.1002/ppp.1884, 2017.

Noetzli, J. and Gruber, S.: Transient thermal effects in Alpine permafrost, Cryosphere, 3, 85–99, https://doi.org/10.5194/tc-3-85-2009, 2009.

Noetzli, J., Gruber, S., Kohl, T., Salzmann, N., and Haeberli, W.: Three-dimensional distribution and evolution of permafrost temperatures in idealized high-mountain topography, Journal of Geophysical Research: Earth Surface, 112, 1–14, https://doi.org/10.1029/2006JF000545, 2007.

Obu, J., Westermann, S., Bartsch, A., Berdnikov, N., Christiansen, H. H., Dashtseren, A., Delaloye, R., Elberling, B., Etzelmüller, B., Kholodov, A., Khomutov, A., Kääb, A., Leibman, M. O., Lewkowicz, A. G., Panda, S. K., Romanovsky, V., Way, R. G., Westergaard-Nielsen, A., Wu, T., Yamkhin, J., and Zou, D.: Northern Hemisphere permafrost map based on TTOP modelling for 2000–2016 at 1FIX ME!!!!km2 scale, Earth-Science Reviews, 193, 299–316, https://doi.org/10.1016/j.earscirev.2019.04.023, 2019.

Parr, C., Sturm, M., and Larsen, C.: Snowdrift Landscape Patterns : An Arctic Investigation, Water Resources Research, 56, https://doi.org/10.1029/2020WR027823, 2020.

Patton, A. I., Rathburn, S. L., and Capps, D. M.: Landslide response to climate change in permafrost regions, Geomorphology, 340, 116–128, https://doi.org/10.1016/j.geomorph.2019.04.029, 2019.

Pellet, C. and Noetzli, J.: Swiss Permafrost Bulletin 2018/2019, Permos 2020 (Swiss Permafrost Monitoring Network), pp. 1–20, https://doi.org/10.13093/permos-2019-01.Cover, 2020.

Phillips, M., Haberkorn, A., Draebing, D., Krautblatter, M., Rhyner, H., and Kenner, R.: Seasonally intermittent water flow through deep fractures in an Alpine Rock Ridge: Gemsstock, Central Swiss Alps, Cold Regions Science and Technology, 125, 117–127, https://doi.org/10.1016/j.coldregions.2016.02.010, 2016.

Porter, C.: ArcticDEM, Version 3, 2018.

Rasmussen, L. H., Zhang, W., Hollesen, J., Cable, S., Christiansen, H. H., Jansson, P. E., and Elberling, B.: Modelling present and future permafrost thermal regimes in Northeast Greenland, Cold Regions Science and Technology, 146, 199–213, https://doi.org/10.1016/j.coldregions.2017.10.011, 2018.

Ravanel, L. and Deline, P.: Climate influence on rockfalls in high-alpine steep rockwalls: The north side of the aiguilles de chamonix (mont blanc massif) since the end of the 'Little Ice Age', Holocene, 21, 357–365, https://doi.org/10.1177/0959683610374887, 2011.

Rico, I., Magnin, F., López Moreno, J. I., Serrano, E., Alonso-González, E., Revuelto, J., Hughes-Allen, L., and Gómez-Lende, M.: First evidence of rock wall permafrost in the Pyrenees (Vignemale peak, 3,298 m a.s.l., 42°46′16′′N/0°08′33′′W), Permafrost and Periglacial Processes, pp. 673–680, https://doi.org/10.1002/ppp.2130, 2021.

Schmidt, J. U., Etzelmüller, B., Schuler, T. V., Magnin, F., Boike, J., Langer, M., and Westermann, S.: Surface temperatures and their influence on the permafrost thermal regime in high Arctic rock walls on Svalbard, The Cryosphere, 15, 1–29, https://doi.org/10.5194/tc-2020-340, 2021.

Stocker-Mittaz, C., Hoelzle, M., and Haeberli, W.: Modelling alpine permafrost distribution based on energy-balance data: a first step, Permafrost and Periglacial Processes, 13, 271–282, https://doi.org/10.1002/ppp.426, 2002.

Strzelecki, M. C., Jaskólski, M. W., and Strzelecki, M. C.: Arctic tsunamis threaten coastal landscapes and communities -Survey of Karrat Isfjord 2017 tsunami effects in Nuugaatsiaq, western Greenland, Natural Hazards and Earth System Sciences, 20, 2521–2534, https://doi.org/10.5194/nhess-20-2521-2020, 2020.

Svennevig, K.: Preliminary landslide mapping in Greenland, GEUS Bulletin, 43, 1–5, 2019.

Svennevig, K., Dahl-Jensen, T., Keiding, M., Peter Merryman Boncori, J., Larsen, T. B., Salehi, S., Munck Solgaard, A., and Voss, P. H.: Evolution of events before and after the 17 June 2017 rock avalanche at Karrat Fjord, West Greenland - A multidisciplinary approach to detecting and locating unstable rock slopes in a remote Arctic area, Earth Surface Dynamics, 8, 1021–1038, https://doi.org/10.5194/esurf-8-1021-2020, 2020.

Svennevig, K., Hermanns, R. L., Keiding, M., Binder, D., Citterio, M., Dahl-Jensen, T., Mertl, S., Sørensen, E. V., and Voss, P. H.: A large frozen debris avalanche entraining warming permafrost ground—the June 2021 Assapaat landslide, West Greenland, Landslides, 19, 2549–2567, https://doi.org/10.1007/s10346-022-01922-7, 2022.

Svennevig, K., Keiding, M., Korsgaard, N. J., Lucas, A., Owen, M., Poulsen, M. D., Priebe, J., Sørensen, E. V., and Morino, C.: Uncovering a 70-year-old permafrost degradation induced disaster in the Arctic, the 1952 Niiortuut landslide-tsunami in central West Greenland, Science of the Total Environment, 859, https://doi.org/10.1016/j.scitotenv.2022.160110, 2023.

Walls, M., Hvidberg, M., Kleist, M., Knudsen, P., Mørch, P., Egede, P., Taylor, G., Phillips, N., Yamasaki, S., and Watanabe, T.: Hydrological instability and archaeological impact in Northwest Greenland: Sudden mass movement events signal new concerns for circumpolar archaeology, Quaternary Science Reviews, 248, 106 600, https://doi.org/10.1016/j.quascirev.2020.106600, 2020.

Walter, F., Amann, F., Kos, A., Kenner, R., Phillips, M., de Preux, A., Huss, M., Tognacca, C., Clinton, J., Diehl, T., and Bonanomi, Y.: Direct observations of a three million cubic meter rock-slope collapse with almost immediate initiation of ensuing debris flows, Geomorphology, 351, 106 933, https://doi.org/10.1016/j.geomorph.2019.106933, 2020.

Westermann, S., Langer, M., Boike, J., Heikenfeld, M., Peter, M., Etzelmüller, B., and Krinner, G.: Simulating the thermal regime and thaw processes of ice-rich permafrost ground with the land-surface model CryoGrid 3, Geoscientific Model Development, 9, 523–546, https://doi.org/10.5194/gmd-9-523-2016, 2016.

Wood, J.: Geomorphometry in LandSerf, Developments in Soil Science, 33, 333–349, https://doi.org/10.1016/S0166-2481(08)00014-7, 2009.

Yamamoto, Y. and Springman, S. M.: Triaxial stress path tests on artificially prepared analogue alpine permafrost soil, Canadian Geotechnical Journal, 56, 1448–1460, https://doi.org/10.1139/cgj-2017-0737, 2019.